Small-angle scattering of dense, polydisperse granular porous media: Computation free of size effects

Sébastien Brisard*
Université Paris-Est, Laboratoire Navier (UMR 8205), CNRS, ENPC, IFSTTAR, F-77455 Marne-la-Vallée, France

Pierre Levitz†
Université Pierre et Marie Curie, CNRS, Laboratoire PECSA, 4 pl. Jussieu, F-75252 Paris, France
(Received 26 April 2012; revised manuscript received 19 December 2012; published 18 January 2013)

Small-angle x-ray and neutrons scattering is a widespread experimental tool for the investigation of the microstructure of random heterogeneous materials. Validation of (computer-generated) model microstructures often requires the numerical computation of the scattering intensity, which must be carried out with great care due to finite size effects. In this paper, a new method for this computation is presented. It is superior to previously existing methods for three reasons: First, it applies to any type of microstructure (not necessarily granular). Second, closed-form expressions of the size effects inherent to the proposed method can be rigorously derived and removed (in this sense, our method is free of size effects). Third, the complexity of the new algorithm is linear and the computation can easily be updated to account for local changes of the microstructure, while most existing algorithms are quadratic and any change of the microstructure requires a full recomputation. The present paper provides full derivation and validation of this method. Application to the computation of the scattering intensity of dense, polydisperse assemblies of spheres is then presented. A new, simple algorithm for the generation of these dense configurations is introduced. Finally, the results are critically reviewed in the perspective of hardened cement pastes.

DOI: 10.1103/PhysRevE.87.013305 PACS number(s): 02.70.−c, 78.70.Ck

I. INTRODUCTION

In materials science, numerical simulation of physical or mechanical phenomena in confined spaces (such as diffusive transport, convective transport, or macroscopic deformation under applied macroscopic stress) often requires a full three-dimensional (3D) geometrical model of the heterogeneous material under consideration.

Since few experimental techniques provide direct access to the microstructure, one is often reduced to generating a synthetic, "realistic" microstructure, based on some knowledge of the material. Two approaches can be adopted to carry out this generation.

In mimetic simulations, an attempt is made at reproducing the physical and/or chemical phenomena involved in the elaboration of the real material. Early examples of such approaches are the generation of model silica aerogels by diffusion-limited cluster-cluster aggregation [1] and model porous glasses by molecular dynamics simulations [2,3].

An alternative approach is the reconstruction of 3D models from limited microstructural information. In this approach, available experimental characterizations such as two-point correlation functions are used as constraints for the numerical model to be generated, the resulting cost function being minimized by, e.g., simulated annealing [4–6], maximization of the entropy [7] or genetic algorithms [8]. Reverse [9] and hybrid reverse [10] Monte Carlo techniques can also be considered as constrained reconstructions.

Regardless of the actual approach used to create the model, consistency with all available experimental characterizations of the real material must subsequently be verified in order to assess the reliability of the model.

Small-angle x-ray and neutron scattering experiments are attractive tools for the investigation of the microstructure of disordered media. Indeed, they operate on macroscopic samples and provide quantitative 3D information at length scales between 1 and 100 nm, while keeping sample preparation to a minimum. These experiments are therefore often used to carry out the validation of generated model geometries. For example, the structure factor (which is closely related to the scattering intensity) of silica aerogels is computed *a posteriori* in Ref. [1]. In Ref. [10], the reconstruction of porous carbons results from the minimization of a hybrid energy, made of the true energy of the system and the discrepancy between the actual and expected structure factors. In Ref. [11], reconstruction of amorphous material models is constrained by the experimental structure factor and gas adsorption data. In the last two examples, the structure factor constrains the reconstruction; it must therefore be computed at each step of the optimization algorithm.

Obviously, checking the computational model against experimental scattering intensity data requires that the small-angle scattering spectrum of this model be computed. Such a computation is generally difficult, since the practical size of model microstructures is rather small compared to real samples. This limitation induces cutoff effects in real space, which in turn result in many artifacts in Fourier space (where the small-angle scattering experiment actually takes place).

In order to control these artifacts, nontrivial techniques must be invoked to carry out the computation (see the review in Sec. II of this paper). However, Fig. 1 shows that some artifacts remain, even with existing state-of-the-art techniques. For dense, polydisperse configurations, which are addressed in this paper, these artifacts are even more pronounced.

*sebastien.brisard@ifsttar.fr
†pierre.levitz@upmc.fr

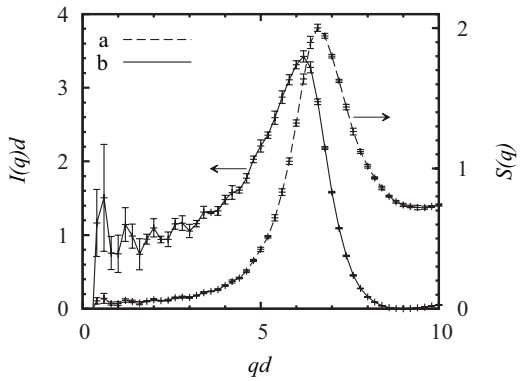

FIG. 1. Even for loose packings of equilibrium monodisperse hard spheres, state-of-the art calculations of the scattering intensity can lead to spurious oscillations at low q. In the present example, four configurations of 4000 hard spheres, with density $f = 0.4$ (volume fraction of solid) are considered. The average structure factor $S(q)$ (a) is computed with the method of Salacuse *et al.* [12]. The result is very satisfactory, even at low q. This is not true of the scattering intensity $I(q)$ (b); indeed, multiplication by the modulus squared of the form factor amplifies the low-q oscillations. Both q and $I(q)$ have been made dimensionless through multiplication by the diameter d of the particles; furthermore, $\Delta\rho = 100d^{-2}$.

This led us to derive a new technique for the computation of the small-angle scattering spectrum of a model microstructure. This method is presented in Sec. III. The resulting spectrum is not free of artifacts; however, these artifacts are controlled, since they result in the true scattering intensity being convolved with a known kernel. Besides, a rigorous method is proposed for their removal. The new method is general in the sense that it applies to any type of geometry. In the present paper, it is specialized to granular media and validated against reference data computed on very large systems.

In Sec. IV, the scattering intensity of dense polydisperse (log-normally distributed) granular media is then computed with this new, validated method. A simple but robust method is first proposed for the generation of the configurations (see Sec. IV A). It is shown that even for relatively wide particle-size distributions, the resulting spectra exhibit a marked correlation peak.

Section V closes this paper with a discussion on the scattering intensity of cementitious materials. The microstructure of calcium-silicate hydrates C–S–H, one of the main hydration products of cement pastes, is still a matter of debate (in the remainder of this paper, standard notation from the cement industry will be adopted: C–S–H is a shorthand for calcium-silicate hydrate, with C ≡ CaO, S ≡ SiO_2, H ≡ H_2O). Among the numerous models which can be found in the literature, the so-called globular model is probably the most popular. Based on small-angle scattering experiments by neutrons [13,14], this model describes the C–S–H phase as an assembly of near-spherical particles, about 5 nm in diameter. Over the years, it has become overwhelmingly popular and has given rise to a colloidal model of C–S–H [15–17]. The interest for this model has recently been renewed, since other experimental results, such as nano-indentation [18–20], or molecular simulations [21], can be interpreted in the light of the colloidal model of C–S–H. Our analysis suggests that only a very wide globule size distribution can account for the typical small-angle scattering spectrum of cement pastes (see Fig 16). This raises the question of the origin of such a wide size distribution.

II. COMPUTATION OF SCATTERING INTENSITY: STATE OF THE ART

Even with efficient procedures (see, e.g., Sec. IV A), computer generated numerical samples are necessarily of very limited extent. In the present work, the typical size of the simulation box is about twenty times the average size of the particles. This is much smaller than the macroscopic samples usually considered in real small-angle scattering experiments, and pronounced boundary effects are therefore to be expected.

Several methods have been proposed in the past to reliably compute the scattering intensity of a numerical sample. These methods are reviewed in Sec. II B, where it is shown that they do not fulfill the requirements of the present work.

First, in Sec. II A, the general equations governing small-angle scattering of x-rays (SAXS) and neutrons by heterogeneous media are recalled. We do not intend to provide a full account of the small-angle scattering theory; only the essential equations to be used in the remainder of this paper are gathered here (the reader is referred to standard text books for a more thorough review; e.g., Refs. [22,23]).

A. General equations

In a small-angle scattering experiment, the amplitude A of the scattered wave is proportional to the Fourier transform of the local scattering-length density ρ

$$A(\boldsymbol{q}) = \int_{\boldsymbol{x}\in\Omega} \rho(\boldsymbol{x}) \exp(-i\boldsymbol{q}\cdot\boldsymbol{x}) d^3\boldsymbol{x}, \tag{1}$$

where $\boldsymbol{q}$ is the scattering vector, and $\Omega \subset \mathbb{R}^3$ is the domain occupied by the sample; all prefactors have been omitted because they are irrelevant to the present work. The absolute scattered intensity $I(\boldsymbol{q})$ is then proportional to the square of the modulus of the amplitude

$$I(\boldsymbol{q}) = \lim_{V\to+\infty} \frac{1}{V} A(\boldsymbol{q}) A^*(\boldsymbol{q}), \tag{2}$$

where $V = |\Omega|$ is the volume of the sample, and the above limit corresponds to the thermodynamic limit.

Following Debye *et al.* [24], it is convenient to introduce the fluctuations $\eta(\boldsymbol{x}) = \rho(\boldsymbol{x}) - \langle\rho\rangle$ of the scattering-length density, where angle brackets denote ensemble averages. Then Eq. (1) reads

$$A(\boldsymbol{q}) = \int_{\boldsymbol{x}\in\Omega} \eta(\boldsymbol{x}) \exp(-i\boldsymbol{q}\cdot\boldsymbol{x}) d^3\boldsymbol{x} + \langle\rho\rangle \int_{\boldsymbol{x}\in\Omega} \exp(-i\boldsymbol{q}\cdot\boldsymbol{x}) d^3\boldsymbol{x}.$$

We note that in the above equation, the last term depends only on the shape of the sample Ω. It is usually omitted [25], since for samples large enough, it is negligible except for very small values of $\boldsymbol{q}$ (it effectively reduces to a Dirac generalized function for infinitely large samples), which cannot be reached

experimentally. It is therefore customary to write

$$A(\boldsymbol{q}) = \int_{\boldsymbol{x}\in\Omega} \eta(\boldsymbol{x}) \exp(-i\boldsymbol{q}\cdot\boldsymbol{x}) d^3\boldsymbol{x}. \tag{3}$$

In "numerical experiments," the size of the sample Ω can no longer be considered as infinitely larger than the characteristic length scale of the heterogeneities. Equations (1) and (3) are therefore not equivalent; this point will be addressed in Sec. III B.

Gathering Eqs. (2) and (3), and using the Wiener-Kintchine theorem, it is finally found that

$$I(\boldsymbol{q}) = \langle \eta^2 \rangle \int_{\boldsymbol{r}\in\mathbb{R}^3} \gamma(\boldsymbol{r}) \exp(-i\boldsymbol{q}\cdot\boldsymbol{r}) d^3\boldsymbol{r}, \tag{4}$$

where $\gamma(\boldsymbol{r})$, first introduced by Debye *et al.* [24], is the normalized autocorrelation function of the fluctuations $\eta(\boldsymbol{x})$

$$\begin{aligned}\gamma(\boldsymbol{r}) &= \frac{1}{\langle \eta^2 \rangle} \langle \eta(\boldsymbol{x}) \eta(\boldsymbol{x}+\boldsymbol{r}) \rangle \\ &= \frac{1}{\langle \eta^2 \rangle} \lim_{V\to+\infty} \frac{1}{V} \int_{\boldsymbol{x}\in\Omega} \eta(\boldsymbol{x}) \eta(\boldsymbol{x}+\boldsymbol{r}) d^3\boldsymbol{x}.\end{aligned} \tag{5}$$

In absolute scale, the scattering intensity appears as the Fourier transform of the autocorrelation of the scattering-length density fluctuations. In numerical experiments, because of the limited size of the sample, $\gamma(\boldsymbol{r})$ cannot be computed for large values of the separation $r = |\boldsymbol{r}|$ (typically, for $r > L/2$, where L is the size of the simulation box). It is therefore not possible to compute reliably its Fourier transform $\hat{\gamma}(\boldsymbol{q}) = I(\boldsymbol{q})/\langle \eta^2 \rangle$ for small values of $q = |\boldsymbol{q}|$ (typically $q \leqslant s\pi/L$, where s is of the order of the unity).

B. Review of existing methods

In the present section, we review existing methods for the computation of the scattering intensity of granular media. For this type of microstructures, the following expression of the scattering amplitude $A(\boldsymbol{q})$ is generally preferred over Eq. (3):

$$A(\boldsymbol{q}) = \sum_{\beta} \Delta\rho_\beta v_\beta F_\beta(\boldsymbol{q}) \exp(-i\boldsymbol{q}\cdot\boldsymbol{x}_\beta), \tag{6}$$

where the sum is extended to all particles in the sample Ω, v_β is the volume of particle β centered at $\boldsymbol{x}_\beta$, $\Delta\rho_\beta = \rho_\beta - \rho_{\text{fluid}}$ is its scattering length density contrast (ρ_β is the scattering-length density of particle β, ρ_{fluid} is the scattering-length density of the saturating fluid), and $F_\beta(\boldsymbol{q})$ is its form factor [25]. For spherical particles,

$$F_\beta(\boldsymbol{q}) = 3\frac{\mathrm{j}_1(qa_\beta)}{qa_\beta}, \quad \mathrm{j}_1(x) = \frac{\sin x - x\cos x}{x^2}, \tag{7}$$

where $q = |\boldsymbol{q}|$, a_β is the radius of particle β, and j_1 denotes the spherical Bessel function of the first order and first kind.

Direct implementation of Eq. (6) (where the sum is now extended to all particles in the much smaller simulation box $\mathcal{U}$), followed by the application of Eq. (2) (where no limit is taken), defines what will be called below the basic method. For isotropic, monodisperse configurations, the relevant formulas read

$$I(q) = \Delta\rho^2 f v F(q)^2 S(q), \tag{8a}$$

$$S(q) = \frac{1}{N} \sum_{\beta,\gamma=1}^{N} \mathrm{H}(r_\mathrm{c} - r_{\beta\gamma}) \mathrm{sinc}(qr_{\beta\gamma}), \tag{8b}$$

where N is the total number of particles in $\mathcal{U}$, f is their volume fraction, $r_{\beta\gamma}$ is the center-to-center distance of particles β and γ, $r_\mathrm{c} = L/2$ is the cutoff distance (the maximum meaningful correlation length), and H is the Heaviside step function. Although simple, this procedure leads to pronounced artifacts at low q.

Size effects are at the origin of these artifacts. Salacuse *et al.* [12] identify two types of such effects (see also Refs. [26,27]). First, fixing the total number of particles in the simulation box leads to so-called explicit (or ensemble) size effects. Second, boundary conditions lead to so-called implicit (or anomalous) size effects. Indeed, boundaries of the simulation box in real space introduce a cutoff which can, if not handled properly, lead in Fourier space to large oscillations and unexpected increase at low q (see also Fig. 2(a) in Ref. [28], and Ref. [29]).

Anomalous size effects are a well-known issue within the diffraction community [30], where window functions are widely used as apodizing filters. For peaked spectra, apodizing filters perform very satisfactorily, because the location of each peak is but little affected by the filter. For spectra such as those shown in Figs. 16 and 19 (with no peaks), the overall shape is significantly modified by the filter, in a way which is difficult to quantify. Therefore, apodizing filters are not a reliable remedy in the present, general case.

Throughout the years, many methods have been proposed to deal with anomalous size effects [12,28,31,32]. For monodisperse distributions, Salacuse *et al.* [12,32] introduce the following correction to Eq. (8b):

$$S(q) = \frac{1}{N} \sum_{\beta,\gamma=1}^{N} \mathrm{H}(r_\mathrm{c} - r_{\beta\gamma}) \mathrm{sinc}(qr_{\beta\gamma}) - 3nv_\mathrm{c} \frac{\mathrm{j}_1(qr_\mathrm{c})}{qr_\mathrm{c}} \tag{9}$$

($n = N/V$ is the number density of particles, v_c is the volume of the sphere with radius r_c). This procedure has been used successfully by Moe and Ediger [33], and more recently by Donev *et al.* [34].

The complemented system approach recently proposed by Lajovic *et al.* [29] can be seen as an extension of this procedure to polydisperse systems. It is derived by assuming that all correlations vanish for distances greater than r_c. More precisely, the unknown value of the pair correlation function $g_{AB}(r)$ (where A and B are two types of atoms) is replaced with 1 for $r \geqslant r_\mathrm{c}$. The resulting formula reads

$$\begin{aligned}I(q) = &\frac{1}{V} \sum_{\beta,\gamma=1}^{N} b_\beta(q) b_\gamma(q) \mathrm{H}(r_\mathrm{c} - r_{\beta\gamma}) \mathrm{sinc}(qr_{\beta\gamma}) \\ &- 3v_\mathrm{c} \frac{\mathrm{j}_1(qr_\mathrm{c})}{qr_\mathrm{c}} \left[\frac{1}{V} \sum_{\beta=1}^{N} b_\beta(q) \right]^2,\end{aligned} \tag{10}$$

with $b_\beta(q) = \Delta\rho_\beta v_\beta F_\beta(q)$. It can readily be verified that, for monodisperse systems, Eq. (10) coincides with Eqs. (8a) and (9).

In the reciprocal lattice approach, Frenkel *et al.* [31] use an unmodified version of the basic method, but only for selected values of the vector $\boldsymbol{q}$; namely,

$$\boldsymbol{q}_{hkl} = \frac{2\pi}{L}(h\boldsymbol{e}_1 + k\boldsymbol{e}_2 + l\boldsymbol{e}_3).$$

Why such a selection of $\boldsymbol{q}$ efficiently removes anomalous size effects is explained by the fact that the form factor of the (cubic) simulation box is null for each $\boldsymbol{q}_{hkl}$ [see Eq. (19), where the unit cell $\mathcal{U}$ should be taken as window $\mathcal{W}$].

This procedure is slightly superior to the correction (9) proposed by Salacuse *et al.* [12], because it also applies to polydisperse distributions. However, in the method of Frenkel *et al.* [31], only very few directions of the scattering vector $\boldsymbol{q}$ are sampled at low q. This affects the accuracy of the subsequent isotropic averaging of $I(\boldsymbol{q})$ and contrived us not to use this method because we require the computation to be as reliable as possible at low q.

For the sake of completeness, the method developed by Tomšič *et al.* [28] should be cited. However, the authors agree that, with this method, "the numerical suppression of truncation artifacts is found to be less than optimal" [29].

From the above review, it would seem that only the complemented system approach [29] would suit our needs for a method which applies to polydisperse systems, is accurate at small q, and removes unwanted size effects.

However, it must be pointed out that this approach only addresses anomalous size effects, while ensemble size effects are not considered. Ensemble size effects also result in spurious oscillations at low q. Averaging the spectra over many configurations usually solves this issue; for example, Fig 1 in Ref. [29] shows an average over 100 configurations. In many instances, though, only one configuration is available for the computation, and averaging becomes impossible. In the method we propose in Sec. III, this problem is overcome by the introduction of a window $\mathcal{W}$, which effectively samples the unique configuration $\mathcal{U}$ (see Sec. III A).

Moreover, extension of Eq. (10) to general (not necessarily granular) heterogeneous media [defined by the map $\boldsymbol{x} \mapsto \eta(\boldsymbol{x})$] is unclear, while the method proposed in Sec. III applies to any type of microstructures.

To close this review, it should also be noted that all above methods involve double sums because they are based on the direct computation of the scattering *intensity*. Therefore, the required CPU time grows as N^2 (see Fig. 5 of Ref. [29]). Also, even the slightest update of the system (e.g., moving only one particle) requires a full recomputation.

By contrast, our method is based on the computation of the scattering *amplitude*; only simple sums are involved, and the required CPU time grows as N. Besides, slight changes of the system are easily accommodated; for example, moving a particle only requires subtraction of its former contribution to the total amplitude, and addition of its new contribution. This simple update procedure is highly desirable in reconstructions where the scattering intensity is used as a constraint (and must therefore be computed at each iteration of the optimization algorithm).

III. MASTERING FINITE SIZE EFFECTS

In this section, we propose a new method for the computation of the scattering intensity of heterogeneous media. This method explicitly accounts for finite size effects and allows for polydispersity and fine sampling of the directions of $\boldsymbol{q}$. It shares some similarities with the periodograms [35] commonly used in signal analysis.

Section III A provides an overview of the method. Section III B discusses the removal of implicit size effects. The proposed method is very general; in Secs. III C and III D, it is specialized to isotropic and granular media. Then, Sec. III E deals with explicit size effects. Finally, the method is validated in Sec. III F.

A. Overview of method

Instead of considering the simulation box $\mathcal{U}$ (unit cell) as a whole, we consider only the matter contained in a three-dimensional "window."

More precisely, let $\mathcal{W} \subset \mathbb{R}^3$ be the so-called window, with characteristic function $\boldsymbol{x} \mapsto w(\boldsymbol{x})$. $\boldsymbol{x} \in \mathcal{U}$ being fixed, we compute the Fourier transform of η inside the window $\mathcal{W}$ centered at $\boldsymbol{x}$

$$A_{\mathrm{w}}(\boldsymbol{q},\boldsymbol{x}) = \int_{\boldsymbol{y}\in\mathbb{R}^3} w(\boldsymbol{y}-\boldsymbol{x})\eta(\boldsymbol{y})\exp(-i\boldsymbol{q}\cdot\boldsymbol{y})d^3\boldsymbol{y}. \qquad (11)$$

It should be noticed that the integral in the above equation is computed with periodic boundary conditions. Therefore, intersections of the window $\mathcal{W}$ with all periodic images of particle β must be considered, and only that part of particle β which is effectively inside $\mathcal{W}$ is included in the integration process (as illustrated in Fig. 2). This last point makes the above calculation much more involved than Eq. (6), since it precludes the use of closed-form expressions of the form factor F_β.

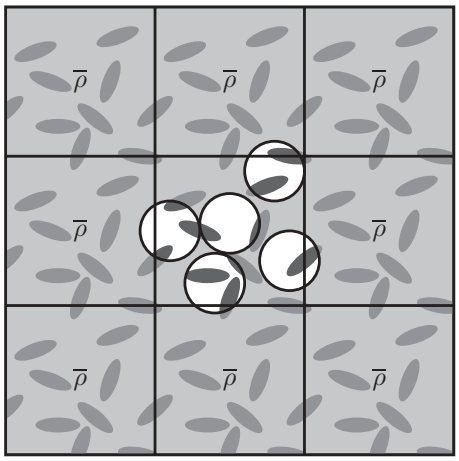

FIG. 2. Illustration of Eq. (11). Four different locations of the window $\mathcal{W}$ are considered (white disks). For each of these locations, only that part of the periodic images of a specific particle is considered, which is contained within the window (in dark gray). It is shown in Sec. III B that using $\eta(\boldsymbol{x})$ instead of $\rho(\boldsymbol{x})$ in Eq. (11) is equivalent to replacing the heterogeneous material outside the current window with an average material (homogeneous scattering length density $\overline{\rho}$).

We then define the intensity $I_w(\boldsymbol{q})$ through the following volume average of the local amplitude $A_w(\boldsymbol{q},\boldsymbol{x})$ over all $\boldsymbol{x} \in \mathcal{U}$:

$$I_w(\boldsymbol{q}) = \frac{1}{|\mathcal{W}|}\frac{1}{|\mathcal{U}|}\int_{\mathcal{U}} |A_w(\boldsymbol{q},\boldsymbol{x})|^2 d^3\boldsymbol{x}, \tag{12}$$

where $|\mathcal{U}|$ ($|\mathcal{W}|$) denotes the volume of the unit cell (the window).

The rationale for defining $I_w(\boldsymbol{q})$ as a volume average is twofold. First, the heterogeneous media under consideration are statistically homogeneous. All points $\boldsymbol{x}$ being equivalent, there is no reason why the window $\mathcal{W}$ should be centered at a specific point, and all possible locations should be considered. Second, the scattering intensity pattern is the signature of the fluctuations of the local scattering-length density (for example, the intensity at zero angle is proportional to the so-called static compressibility of the material [23], Sec. V C]). Fixing the total number of particles in the simulation box effectively kills these fluctuations for length-scales $\sim L$; this results in ensemble size effects [12]. However, fluctuations at length scales smaller than L are not prevented. Using multiple windows $\mathcal{W}$ captures these fluctuations and explicitly accounts for ensemble size effects.

Indeed, we prove in Appendix A that Eq. (12) is a biased estimate of the true intensity $I(\boldsymbol{q})$, provided that $\mathrm{diam}\mathcal{W} < L/2$. More precisely,

$$I_w(\boldsymbol{q}) = \frac{1}{(2\pi)^3}\int_{\boldsymbol{p}\in\mathbb{R}^3} \hat{\gamma}_w(\boldsymbol{q}-\boldsymbol{p}) I(\boldsymbol{p}) d^3\boldsymbol{p}, \tag{13}$$

where γ_w is the normalized correlation function of the window $\mathcal{W}$ [23], and $\hat{\gamma}_w$ is its Fourier transform [see Appendix A, Eqs. (A4) and (A5)]. From Eq. (13), I_w appears to be the result of the convolution of the desired spectrum I with a known kernel; for this reason, it will be called the *blurred intensity*.

It is interesting to note that the convolution product in Eq. (13) stems from the fact that Eq. (12) is a volume average over all locations of the window $\mathcal{W}$. By contrast, only one location of $\mathcal{W}$ is considered in Sec. II B, with the benefit that a larger window can be used ($\mathrm{diam}\mathcal{W} < L$ instead of $\mathrm{diam}\mathcal{W} < L/2$); the price to pay is unquantified (ensemble) size effects. One of the main contributions of this paper is the proof that these size effects can be rigorously quantified through Eq. (13) when multiple smaller windows are used.

In our implementation of the method outlined above, integral (12) is discretized on a regular grid (typically $8 \times 8 \times 8$): the window $\mathcal{W}$ is centered at each vertex of this grid in turn. For each location of the window, integral (11) is then computed semi-analytically. This leads to an estimate of $I_w(\boldsymbol{q})$. If necessary, sampling over all directions of $\boldsymbol{q}$ then provides an estimate of the isotropic average $I_w(q)$.

How $I(\boldsymbol{q})$ is retrieved from $I_w(\boldsymbol{q})$ is detailed in Sec. III E. In Sec. III B, we first discuss the use of $\eta(\boldsymbol{x})$ in place of $\rho(\boldsymbol{x})$ in Eq. (11); in Secs. III C and III D we then go on to show how the previous expressions can be specialized to particulate, statistically isotropic media.

B. Scattering-length density vs fluctuations of this density

Attention should be drawn to the fact that, in Eq. (11), $A_w(\boldsymbol{q},\boldsymbol{x})$ is defined as the Fourier transform of the fluctuations $\eta(\boldsymbol{x})$ of the scattering-length density. This definition is somewhat counter intuitive, and it would have been more natural to define $A_w(\boldsymbol{q},\boldsymbol{x})$ as the Fourier transform of the scattering-length density $\rho(\boldsymbol{x})$ itself.

While strictly equivalent for very large samples [see the discussion about Eqs. (1) and (3)], these two definitions lead to widely different results in the case of simulation boxes of limited extent. We found that it is essential to use $\eta(\boldsymbol{x})$ and not $\rho(\boldsymbol{x})$ in Eq. (11), because this definition removes most of the implicit size effects induced by the finiteness of the window $\mathcal{W}$. This assertion is justified heuristically below, and a more quantitative illustration can be found in Sec. III F.

We consider a homogeneous system, with uniform scattering length density $\overline{\rho}$. Obviously, for such a system

$$I(\boldsymbol{q}) = 0 \quad \text{and} \quad \eta(\boldsymbol{x}) = 0,$$

and we find, as expected, from Eqs. (11) and (12),

$$A_w(\boldsymbol{q},\boldsymbol{x}) = 0 \quad \text{and} \quad I_w(\boldsymbol{q}) = 0.$$

However, if $A_w(\boldsymbol{q},\boldsymbol{x})$ had been defined as the Fourier transform of the scattering-length density $\rho(\boldsymbol{x})$, instead of its fluctuations $\eta(\boldsymbol{x})$, we would have found

$$A_w(\boldsymbol{q},\boldsymbol{x}) = \overline{\rho}|\mathcal{W}| \exp(-i\boldsymbol{q}\cdot\boldsymbol{x}) F_w(q),$$

where F_w is the form factor of the window $\mathcal{W}$:

$$F_w(\boldsymbol{q}) = \frac{1}{|\mathcal{W}|}\int_{\boldsymbol{x}\in\mathcal{W}} \exp(-i\boldsymbol{q}\cdot\boldsymbol{x}) d^3\boldsymbol{x}. \tag{14}$$

The resulting scattering spectrum would then have been given by

$$I_w(q) = \overline{\rho}^2 |\mathcal{W}| F_w(q)^2. \tag{15}$$

The above incorrect expression exhibits marked, unwanted oscillations at low q which are merely the signature of the window $\mathcal{W}$ and do not reflect the internal microstructure of the medium contained in $\mathcal{W}$. This was already noted by Tomšič *et al.* [28].

The proposed replacement of the scattering-length density $\rho(\boldsymbol{x})$ with its fluctuations $\eta(\boldsymbol{x})$ in Eq. (11) is equivalent to embedding the spherical window $\mathcal{W}$ in a homogeneous, average medium. Indeed, since $\eta(\boldsymbol{x}) = \rho(\boldsymbol{x}) - \overline{\rho}$, Eq. (11) also reads

$$A_w(\boldsymbol{q},\boldsymbol{x}) = \int_{\boldsymbol{y}\in\mathbb{R}^3} w(\boldsymbol{y}-\boldsymbol{x})\rho(\boldsymbol{y}) \exp(-i\boldsymbol{q}\cdot\boldsymbol{y}) d^3\boldsymbol{y} - \int_{\boldsymbol{y}\in\mathbb{R}^3} w(\boldsymbol{y}-\boldsymbol{x})\overline{\rho} \exp(-i\boldsymbol{q}\cdot\boldsymbol{y}) d^3\boldsymbol{y}.$$

From Babinet's principle, $w(\boldsymbol{y}-\boldsymbol{x})$ in the second integral can be replaced (up to a Dirac generalized function) with $-[1-w(\boldsymbol{y}-\boldsymbol{x})]$:

$$A_w(\boldsymbol{q},\boldsymbol{x}) = \int_{\boldsymbol{y}\in\mathbb{R}^3} w(\boldsymbol{y}-\boldsymbol{x})\rho(\boldsymbol{y}) \exp(-i\boldsymbol{q}\cdot\boldsymbol{y}) d^3\boldsymbol{y} + \int_{\boldsymbol{y}\in\mathbb{R}^3} [1-w(\boldsymbol{y}-\boldsymbol{x})]\overline{\rho} \exp(-i\boldsymbol{q}\cdot\boldsymbol{y}) d^3\boldsymbol{y}.$$

The quantity in square brackets, $[1-w(\boldsymbol{y}-\boldsymbol{x})]$, is nonzero only for points outside the window $\mathcal{W}$. Therefore, the second

term can be understood as the contribution to the total scattered amplitude of the exterior domain, filled with a homogeneous, average material.

To close this section, it should be noted that Lajovic *et al.* [29] also claim that the complemented system approach [see Eq. (10) in the present paper] is equivalent to "complementing the missing surroundings of each particle with an average image of the system." In their work, however, the physical properties of this "average" material are unclear, while in the present paper, the uniform scattering-length density of the outside material is clearly the volume average $\overline{\rho}$.

C. Isotropic average of blurred spectrum

In real small-angle scattering experiments, the measured scattering intensity $I(q)$ is usually the isotropic average of the intensity $I(\boldsymbol{q})$ defined in Eq. (2) (with $q = |\boldsymbol{q}|$). Comparing computational to experimental results therefore requires the computation of the following isotropic average:

$$I_{\mathrm{w}}(q) = \frac{1}{4\pi} \int_{|\boldsymbol{n}|=1} I_{\mathrm{w}}(q\boldsymbol{n}) d^2\boldsymbol{n}. \tag{16}$$

Although not mandatory, selection of a spherical window $\mathcal{W}$ is then natural, since such a choice means that no specific direction is preferred throughout the computation. For this particular choice of the window $\mathcal{W}$, the following integral relationship can be derived from Eq. (13) (see the proof in Appendix B):

$$q I_{\mathrm{w}}(q) = \frac{6R}{\pi} \int_0^{+\infty} \{\varphi[2R(q-p)] - \varphi[2R(q+p)]\} \times p I(p) dp, \tag{17}$$

where $I(q)$ [$I_{\mathrm{w}}(q)$] is the isotropic average of the true (blurred) spectrum, R is the radius of the spherical window $\mathcal{W}$, and the kernel φ is given by

$$\varphi(t) = \frac{1}{t^4}\left(1 + \frac{t^2}{2} - \cos t - t \sin t\right). \tag{18}$$

The occurrence in Eq. (17) of the length scale R shows that size effects are explicitly accounted for in the present method. It should be emphasized that Eq. (17) is rigorous. In other words, similarly to all other existing methods for computing the scattering intensity, ours is not devoid of size effects. However, contrary to all other existing methods, we *know* precisely what these effects are.

To close this section, it is reminded that the diameter of the window must not be larger than half the size of the unit cell. In other words, we must have in the present case $R < L/4$. This condition ensures that no particle is correlated with one of its own periodic images. All computations presented in this work were carried out with spherical windows, with maximum allowable size $R = \mathrm{diam}\mathcal{W}/2 = L/4$.

D. Specialization of method to granular media

The method introduced in the present work is general, because it requires only the local map $\boldsymbol{x} \mapsto \eta(\boldsymbol{x})$. However, the general equation (11) can be specialized to particulate media, for which it is convenient to introduce the contrast in scattering-length density

$$A_{\mathrm{w}}(\boldsymbol{q},\boldsymbol{x}) = \sum_{\beta=1}^{N} \Delta\rho_\beta \int_{\boldsymbol{y}\in\omega_\beta} w(\boldsymbol{y}-\boldsymbol{x}) \exp(-i\boldsymbol{q}\cdot\boldsymbol{y}) d^3\boldsymbol{y} - \Delta\overline{\rho}|\mathcal{W}| \exp(-i\boldsymbol{q}\cdot\boldsymbol{x}) F_{\mathrm{w}}(\boldsymbol{q}), \tag{19}$$

where the notations introduced in Sec. II have been adopted, ω_β is the domain occupied by particle β and its periodic images, and F_{w} is given by Eq. (14). $\Delta\overline{\rho}$ denotes the volume average of $\Delta\rho$ on the *entire* simulation box:

$$\Delta\overline{\rho} = \sum_{\beta=1}^{N} \frac{v_\beta}{|\mathcal{U}|} \Delta\rho_\beta.$$

If particle β is completely included in the window $\mathcal{W}$ (centered at $\boldsymbol{x}$), then the integral in Eq. (19) reduces to $v_\beta F_\beta(\boldsymbol{q})$, for which closed-form expressions exist for many particle shapes [see Eq. (7) for spherical particles]. For the particles which cross the boundary of the window, this integral must generally be computed numerically. Efficient techniques can be implemented for spherical particles (see Appendix C).

E. Deconvolution of blurred spectrum

It must be emphasized again that the method introduced in Sec. III A does not provide a direct estimate of the true scattering intensity $I(\boldsymbol{q})$. Indeed, the blurred spectrum $I_{\mathrm{w}}(\boldsymbol{q})$ is the result of the convolution of the true spectrum $I(\boldsymbol{q})$ with a known kernel [see Eq. (13)]. The purpose of this section is to show how $I(\boldsymbol{q})$ can be retrieved from the computed $I_{\mathrm{w}}(\boldsymbol{q})$.

In the remainder of this paper, we will assume that the window $\mathcal{W}$ used to compute the blurred spectrum $I_{\mathrm{w}}(\boldsymbol{q})$ is spherical. Also, we will concentrate on the determination of the isotropic average $I(q)$ from the isotropic average of $I_{\mathrm{w}}(q)$ via identity (17).

The mathematical analysis of this identity is greatly simplified if $q \mapsto I(q)$ is first symmetrized about the origin. In what follows, we will therefore adopt the convention $I(q) = I(-q)$, $q < 0$. Introducing

$$J(q) = qI(q) \quad \text{and} \quad J_{\mathrm{w}}(q) = qI_{\mathrm{w}}(q), \tag{20}$$

Eq. (17) then reduces to a simple convolution product

$$J_{\mathrm{w}}(q) = \int_{-\infty}^{+\infty} k(q-p) J(p) dp \quad \text{with} \quad k(q) = \frac{6R}{\pi}\varphi(2Rq)$$

or, in a more compact form ("$*$" denoting convolution product)

$$J_{\mathrm{w}}(q) = (k * J)(q). \tag{21}$$

Taking the Fourier transform of both sides, we then find

$$\hat{J}_{\mathrm{w}}(x) = \hat{k}(x)\hat{J}(x), \tag{22}$$

with

$$\hat{J}(x) = \int_{-\infty}^{+\infty} J(q) \exp(-iqx) dx,$$

and similar relations for $\hat{J}_{\mathrm{w}}$ and $\hat{k}$. From Eq. (22) it would seem that retrieving I (the quantity of interest) from I_{w} (the quantity effectively computed) reduces to a straightforward division in Fourier space. In fact, the situation is more complex, since $\hat{k}(x) = 0$ for $|x| > 2R$ [see Eqs. (D1) and (D2) in Appendix D].

Therefore, the high-x values of $\hat{J}$ cannot be retrieved from the calculation presented here; this is consistent with the fact that we are working on a finite size simulation (where large correlation lengths cannot be reached).

To sum up, inverting Eq. (17) is not possible because we are missing information at high x, and Eq. (17) admits multiple solutions. To compensate for this missing information, we must introduce some prior knowledge about $I(q)$ in order to select a reasonable solution for $I(q)$. In mathematical terms, this is known as regularization. In the present work, we used standard Tikhonov regularization (see, e.g., Ref. [36]) combined with the discrepancy principle. The overall procedure is detailed in the remainder of this section.

We first note from Eq. (22) that $J_{\mathrm{w}}(q)$ is band limited, which has deep implications for the sampling of $J_{\mathrm{w}}(q)$ as well as the calculation of its Fourier transform.

The Shannon-Nyquist theorem indeed states that the band-limited function J_{w} can be fully reconstructed from its sampling at evenly spaced values $q_m = m\pi/(2R)$ ($m \in \mathbb{Z}$):

$$J_w(q) = \sum_{m=-\infty}^{+\infty} J_w\left(\frac{m\pi}{2R}\right)\mathrm{sinc}(2Rq - m\pi) \tag{23}$$

$$= \sum_{m=1}^{+\infty} 2m\pi(-1)^m J_w\left(\frac{m\pi}{2R}\right)\frac{\sin(2Rq)}{(2Rq)^2 - (m\pi)^2}, \tag{24}$$

where the second equality accounts for J_{w} being an odd function.

Equation (23) is essential from the practical point of view, since it indicates how the blurred spectrum should be reliably sampled. In the present work, the M first values of I_{w} were first sampled at the required spacing. Multiplication by the corresponding value of q then provided the finite series

$$J_{\mathrm{w}}(0), J_{\mathrm{w}}\left(\frac{\pi}{2R}\right), \ldots, J_{\mathrm{w}}\left[\frac{(M-1)\pi}{2R}\right],$$

from which J_{w} was fully reconstructed by means of the interpolation formula (24), where the infinite sum was truncated at $m = M$. Such a truncation is meaningful (provided M is large enough), since $q^4 I_{\mathrm{w}}(q) \to$ const. as $q \to +\infty$ (Porod regime); therefore, $q^3 J_{\mathrm{w}}(q) \to$ const. as $q \to +\infty$.

Another implication of the Shannon-Nyquist theorem is the possibility to compute *exactly* the Fourier transform of J_{w} from its sampled values. Indeed, from the known Fourier transform of the sine cardinal function, combined with Eq. (23), we find

$$\hat{J}_{\mathrm{w}}(x) = \frac{\pi}{2R}\mathrm{rect}\left(\frac{x}{2R}\right)\sum_{m=-\infty}^{+\infty} J_{\mathrm{w}}\left(\frac{m\pi}{2R}\right)\exp\left(-i\frac{m\pi x}{2R}\right)$$

$$= -\frac{i\pi}{R}\mathrm{rect}\left(\frac{x}{2R}\right)\sum_{m=1}^{+\infty} J_{\mathrm{w}}\left(\frac{m\pi}{2R}\right)\sin\left(\frac{m\pi x}{2R}\right), \tag{25}$$

where the second line again results from J_{w} being odd, and

$$\mathrm{rect}(\omega) = \begin{cases} 1 & \text{if } |\omega| < 1 \\ 0 & \text{otherwise.} \end{cases}$$

Truncating the sum in Eq. (25) leads to the approximate formula for $x = 2Rk/M$ ($k = 0, \ldots, M-1$):

$$\hat{J}_{\mathrm{w}}\left(\frac{2Rk}{M}\right) \simeq -\frac{i\pi}{R}\sum_{m=0}^{M-1} J_{\mathrm{w}}\left(\frac{m\pi}{2R}\right)\sin\left(\frac{\pi mk}{M}\right). \tag{26}$$

The above expression can be recognized as the discrete sine transform of the finite data series $J_{\mathrm{w}}(0), \ldots, J_{\mathrm{w}}[(M-1)\pi/(2R)]$. Furthermore, the $J_{\mathrm{w}}[m\pi/(2R)]$ (therefore, the *full* description of J_w) can be retrieved from the $\hat{J}_{\mathrm{w}}(2Rk/M)$ by inverse discrete sine transform:

$$J_{\mathrm{w}}\left(\frac{m\pi}{2R}\right) \simeq \frac{2iR}{M\pi}\sum_{k=0}^{M-1} \hat{J}_{\mathrm{w}}\left(\frac{2Rk}{M}\right)\sin\left(\frac{\pi mk}{M}\right). \tag{27}$$

Both direct and inverse discrete sine transforms are computed by means of the fast sine transform.

With these preliminary results in hand, it is now possible to introduce the procedure we used to perform the deconvolution of Eq. (17). As already stated, additional constraints (prior knowledge) must be imposed on the solution to be selected for inversion of problem (17) to be possible. One such additional constraint is to search for a band-limited solution J. This is a reasonable assumption, since neglecting high correlation lengths leads to a smoother solution; besides, Eq. (22) shows that high correlation length modes of J cannot be retrieved from J_{w} [some data is lost through the convolution product (21)].

In theory, requiring $J(q)$ to be band limited makes it uniquely determined, since its Fourier transform is given by

$$\hat{J}(x) = \begin{cases} \frac{\hat{J}_{\mathrm{w}}(x)}{\hat{k}(x)} & \text{if } |x| < 2R \\ 0 & \text{otherwise.} \end{cases}$$

In practice, however, this constraint is not sufficient. Indeed, division by $\hat{k}$ tends to amplify high correlation length modes of J_{w} [since $\hat{k}(x) \to 0$ as $|x| \to 2R$]. These modes are corrupted by numerical noise, which results in spurious oscillations of $J(q)$ (particularly at low q).

In the present work, Tikhonov regularization was used in order to dampen these oscillations. A full description of this widely used technique is beyond the scope of this paper (see, for example, Ref. [36] and references therein). Suffice it to say that in this approach, J is defined as the minimizer of the following functional:

$$\|k * J - J_{\mathrm{w}}\|_2^2 + \lambda^2\|J\|_2^2, \tag{28}$$

rather than the exact solution of Eq. (21). More details on the selection of the user-specified regularization parameter λ are provided below.

The solution to the above optimization problem is explicit in Fourier space. Indeed, Parseval's identity shows that minimizing Eq. (28) is equivalent to minimizing

$$\|\hat{k}\hat{J} - \hat{J}_{\mathrm{w}}\|_2^2 + \lambda^2\|\hat{J}\|_2^2 = \int_{-\infty}^{+\infty}[\hat{k}(x)\hat{J}(x) - \hat{J}_{\mathrm{w}}(x)]^2 dx + \lambda^2\int_{-\infty}^{+\infty}\hat{J}(x)^2 dx.$$

The first variation of this functional with respect to $\hat{J}$ reads

$$2\int_{-\infty}^{+\infty}\{[\hat{k}(x)^2+\lambda^2]\hat{J}(x)-\hat{k}(x)\hat{J}_{\mathrm{w}}(x)\}\delta\hat{J}(x)dx,$$

which must be null for any variation $\delta\hat{J}$ of $\hat{J}$. The regularized solution (in the sense of Tikhonov) therefore reads in Fourier space

$$\hat{J}(x)=\frac{\hat{k}(x)}{\hat{k}(x)^2+\lambda^2}\hat{J}_{\mathrm{w}}(x), \tag{29}$$

which shows that J, like J_{w}, is band limited in this approach. Therefore, the Shannon-Nyquist theorem also applies to the reconstructed $J(q)$. In other words, Eqs. (23) and (25)–(27) remain valid if J is substituted to J_{w}, and the whole deconvolution procedure can be summarized as follows:

(1) Compute $I_{\mathrm{w}}[m\pi/(2R)]$ for $m=0,\dots,M-1$ using Eqs. (11) and (12), or Eqs. (19) and (12).

(2) Compute $J_{\mathrm{w}}[m\pi/(2R)]$ for $m=0,\dots,M-1$ using Eq. (20).

(3) Compute $\hat{J}_{\mathrm{w}}(2Rk/M)$ for $k=0,\dots,M-1$ using Eq. (26).

(4) Compute $\hat{J}(2Rk/M)$ for $k=0,\dots,M-1$ using Eq. (29).

(5) Compute $J[m\pi/(2R)]$ for $m=0,\dots,M-1$ using Eq. (27) (where J should be substituted to J_{w}).

(6) Interpolate $J(q)$ for any $0\leqslant q\leqslant(M-1)\pi/(2R)$ using Eq. (24) (again, J should be substituted to J_{w}).

(7) Use Eq. (20) to retrieve $I(q)$ for any $0\leqslant q\leqslant(M-1)\pi/(2R)$.

It is interesting to note that the above deconvolution procedure is based on assumptions similar to the complemented system approach of Lajovic *et al.* [29]. Indeed, reconstructing $J(q)$ as a band-limited signal means that two-point correlations are neglected for $r\geqslant 2R$. However, unlike the complemented system approach, correlations are brought smoothly down to zero [see Eq. (29)], through multiplication by $\hat{k}(x)/[\hat{k}(x)^2+\lambda^2]$, which can be seen as a specially designed apodization filter.

The above procedure requires the selection of a specific value for the regularization parameter λ. Obviously, this should be done as objectively as possible.

Many criteria have been proposed in the past for an objective selection of λ (see, e.g., Ref. [37]); the most frequently used are probably the L-curve criterion [38,39] or the generalized cross-validation criterion [40]. Unfortunately, none of these criteria proved satisfactory for the present application. We therefore resorted to the discrepancy principle [41], which proved more robust but required quantification of the noise level in the input data $I_{\mathrm{w}}[m\pi/(2R)]$.

The discrepancy principle is based on the fact that selecting the regularization parameter λ results from a compromise between fidelity (achieved with small values of λ) and smoothness (achieved with large values of λ) of the reconstructed solution.

In Morozov's view, the largest value of λ achieving the required fidelity of the reconstructed solution must be selected. Fidelity of the solution is assessed by comparison of the residual with the experimental noise; it is required that the former be lower than the latter.

In the present work, four configurations were considered for each value of the polydispersity index α (which will be defined more precisely in section IV A). An estimate of the statistical noise is therefore given by the point-wise standard deviation of the four resulting spectra. Then, the residual is the difference between the initial (blurred) spectrum $I_{\mathrm{w}}(q)$ and the "reblurred" spectrum

$$\frac{(k*J)(q)}{q},$$

where J is the reconstructed solution. The discrepancy principle results in the following simple procedure: λ is progressively increased until the reblurred spectrum is no longer contained within the error bars drawn around I_{w}.

F. Validation of method

The method proposed above must be validated against reference data. To the best of our knowledge, exact expressions of the scattering pattern are not available, even for very simple granular systems. In the present paper, reference scattering patterns are therefore *computed* on systems of monodisperse hard spheres, using the method of Salacuse *et al.* [12]. The computation is carried out on large configurations in order to minimize finite size effects.

Using a standard Monte Carlo procedure [42], we therefore generated two sets of four configurations. So-called large (small) configurations contain $N=108\,000$ ($N=4000$) particles; the volume fraction of the particles is set to $f=0.4$ in both families of configurations.

The method of Salacuse *et al.* [12] was applied to the large ($N=108\,000$ particles) configurations in order to compute the average reference spectrum $I_{\mathrm{ref}}(q)$ shown in Fig. 3, where it is observed that small-q oscillations are kept to a minimum due to the size of the configurations.

The new procedure described above (see Secs. III A to III D) was then applied to the small ($N=4000$ particles) configurations to compute the isotropically averaged blurred spectrum $I_{\mathrm{w}}(q)$. Generating four different configurations allowed us to estimate the numerical noise on $I_{\mathrm{w}}(q)$, which was required

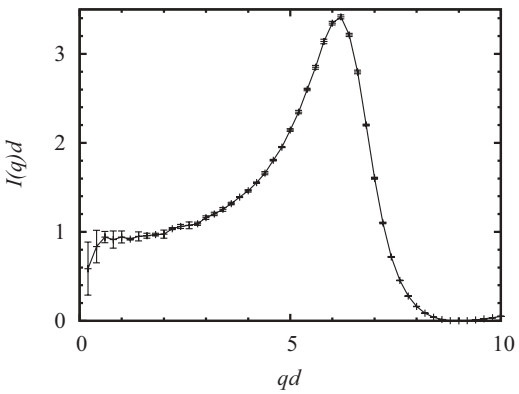

FIG. 3. Average reference spectrum $I_{\mathrm{ref}}(q)$ of the large ($N=108\,000$) configurations of equilibrium monodisperse hard spheres. Due to the size of the configurations considered here, the resulting curve is relatively smooth, even at small q. In Figs. 3 to 8, both q and $I(q)$ have been made dimensionless through multiplication by the diameter d of the particles; furthermore, $\Delta\rho=100d^{-2}$.

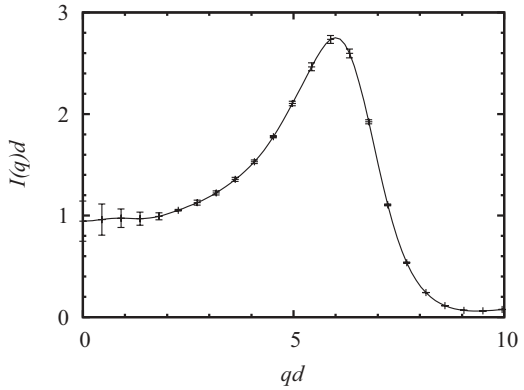

FIG. 4. Average blurred spectrum $I_w(q)$ of the small ($N = 4000$ particles) configurations of equilibrium monodisperse hard spheres.

for a reliable estimation of the regularization parameter λ through the discrepancy principle. The resulting average blurred spectrum is shown in Fig. 4. As expected, the error bars are slightly larger in the low-q region (which corresponds to large correlation lengths).

The deblurred spectrum is then derived from the procedure described in Sec. III E. The resulting curves are shown in Figs. 5 (linear scale) and 6 (logarithmic scale), where they are compared with the reference spectrum $I_{ref}(q)$. It is apparent on Fig. 5 that the location of the first peak is well captured, while its height is slightly underestimated. This was to be expected from the regularization procedure used here (the discrepancy principle is known to overestimate the regularization parameter λ). Nevertheless, the overall agreement between actual and expected spectra is very satisfactory. Figure 6 further confirms this observation, since representation in logarithmic scale shows that the location of the zeros of the spectrum is also captured very accurately.

This application also shows that the method of Salacuse *et al.* [12] is more susceptible to unphysical oscillations at low q than our method. Indeed, computations carried out with this method on small configurations ($N = 4000$ particles) are shown in Fig. 1 (curve b), and should be compared with computations carried out with our method on the same configurations (see Fig. 5, curve b), the latter being less

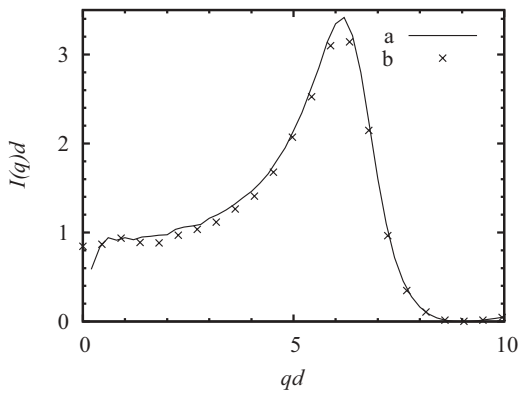

FIG. 5. (a) Reference spectrum $I_{ref}(q)$ and (b) deblurred spectrum $I(q)$ derived from $I_w(q)$ shown in Fig. 4; the agreement is very satisfactory.

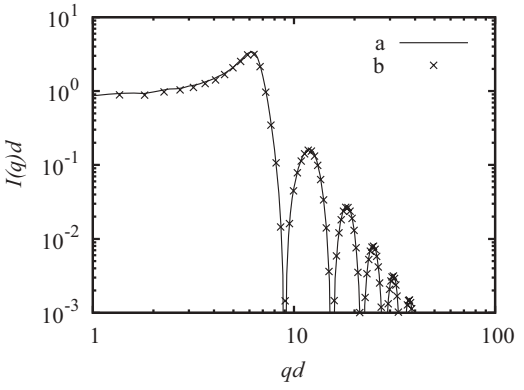

FIG. 6. Same as Fig. 5, but in logarithmic scale.

oscillatory at low q. It seems that this sensitivity to size effects increases with the compacity of the system, as will be illustrated in Sec. IV B (Fig. 12).

To close this section, we again emphasize how important it is to use the fluctuations $\eta(\boldsymbol{x})$ instead of the scattering-length density $\rho(\boldsymbol{x})$ [or equivalently the contrast $\Delta\rho(\boldsymbol{x})$] in formula (11).

This is best demonstrated by performing the same calculation as above, substituting $\rho(\boldsymbol{x})$ to $\eta(\boldsymbol{x})$ (deblurring was not performed because it was not necessary to make our point). The resulting blurred spectrum is shown in Figs. 7 and 8. At low q, the spectrum is dominated by spurious oscillations (see Fig. 7). Figure 8 shows that these oscillations are in fact the contribution of the squared form factor of the window $\mathcal{W}$ [see also Eq. (15)]:

$$\overline{\rho}^2|\mathcal{W}|F_w(q)^2. \tag{30}$$

It is clear from Fig. 7 that $\eta(\boldsymbol{x})$ should indeed be preferred over $\rho(\boldsymbol{x})$ for the computation of the scattering intensity.

This first example confirms the validity of the proposed method, which is applied in Sec. IV to configurations for which the true scattering intensity is not known.

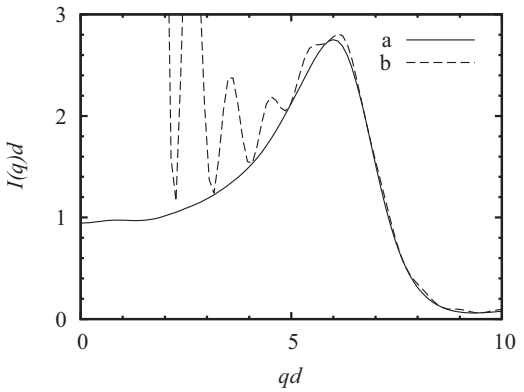

FIG. 7. Average blurred spectrum $I_w(q)$ of the small ($N = 4000$ particles) configurations of equilibrium monodisperse hard spheres, computed with (a) formula (11), and (b) a modified version of this formula, where $\Delta\rho(\boldsymbol{x})$ was substituted to $\eta(\boldsymbol{x})$. The second calculation exhibits spurious oscillations at low q.

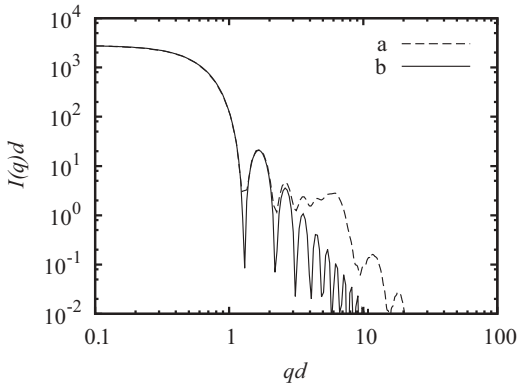

FIG. 8. (a) Average blurred spectrum $I_w(q)$ of the small ($N = 4000$ particles) configurations of equilibrium monodisperse hard spheres and (b) squared form factor of the spherical window, given by Eq. (30). Unlike the curve shown in Fig. 4, $\Delta\rho(\boldsymbol{x})$ was substituted to $\eta(\boldsymbol{x})$ in formula (11). The squared form factor of the window dominates the computed spectrum at low q, leading to an incorrect result.

IV. APPLICATION TO POLYDISPERSE GRANULAR MEDIA

The present section addresses the generation of assemblies of spherical particles with various indices of polydispersity, and low porosity (below 35%). A special procedure is required for the generation of such compact configurations. This procedure is described in Sec. IV A and applied to the generation of twenty compact polydisperse configurations of hard spheres.

In Sec. IV B, the scattering intensity of each of these configurations is computed; the resulting curves are then analyzed.

A. Generation of dense packings of particles

For all assemblies of spheres considered in the present work, the target compacity is fixed at 63.75% and 64% for mono- and polydisperse configurations, respectively; it is therefore comparable to experimentally measured compacities in real cement pastes, while remaining below the so-called random close packing density of monodisperse spherical particles.

Generating assemblies of hard particles near the random close packing density is a difficult task. Most algorithms are based on a molecular dynamics approach, in two [43] and three [44] dimensions. The basic idea is to start from a lose packing, which is densified as the simulation proceeds either by reducing the volume of the simulation box [43–45] or by increasing the size of the particles [46]. This approach is rather effective and flexible; it has been extended to polydisperse assemblies [47] and assemblies of anisotropic particles (e.g., ellipsoids) [48,49]. The downside is the relatively high degree of complexity of these so-called event-driven algorithms.

Although less general, the alternative approach adopted in the present paper leads to very simple numerical codes, while running in a reasonable time. Rather than a molecular dynamics simulation, we carried out a Monte Carlo simulation of an assembly of (possibly polydisperse) spheres in the minimum image convention, aiming at the minimization of the following (nonphysical) "energy":

$$E = \sum_{1\leqslant\beta\neq\gamma\leqslant N} \max\left(\lambda_{\beta\gamma}^{-1} - 1, 0\right), \tag{31}$$

where $\lambda_{\beta\gamma}$ denotes the common scaling factor to be applied simultaneously to both particles β and γ to bring them into (external) contact. If the configuration is admissible, then there is no overlap, and $\lambda_{\beta\gamma} \geqslant 1$, so that the above energy E is rigorously 0.

The simulation is started with a nonadmissible configuration in which the particles are placed randomly (with many overlaps): the initial energy is nonzero. During one cycle of the simulation, each particle in turn is submitted to a random translation, the magnitude of which is controlled by the user. Following the standard Metropolis approach [42,50], the proposed move is accepted with probability

$$\min[\exp(-\beta\Delta E), 1],$$

where ΔE denotes the change in energy incurred by the move under consideration. For physically meaningful energies, β is related to the temperature of the system; in the present case, it has no physical meaning.

In view of minimizing the cost function E given by Eq. (31) using a simulated annealing strategy [51], the β factor is gradually increased, following the "cooling" schedule

$$\beta' = (1 + \epsilon)\beta, \tag{32}$$

where $\epsilon > 0$ (typically ϵ ranges from 0.001 to 0.1), and β' is the new value of the β factor, which is updated every few (typically 4) cycles. It is recalled that, following the terminology of Allen and Tildesley [42], a cycle is completed when each single particle in turn has been submitted to a trial move (both accepted and rejected trials are taken into account in this definition).

The simulation is stopped when the minimum $E = 0$ is reached. It should be noted that the algorithm might fail to converge if the system gets frozen in a local minimum of the energy E; in this case, the simulation is started anew. In order to minimize the number of occurrences of this situation, very dense configurations are obtained in several steps. A first (not too dense) configuration is generated following the above procedure. Then each particle in this first configuration is scaled by the same factor; this effectively increases the compacity of the assembly of particles, but also generates overlaps. Simulated annealing is again invoked to correct these overlaps, resulting in a second (admissible) configuration. The procedure is repeated until the desired compacity is reached. Table I shows an example of this procedure, for the generation of an assembly of 4096 monodisperse hard-spheres; four steps (in other words, four successive Monte Carlo simulations) were necessary in this case to reach the desired compacity $f = 0.6375$.

It should be noted that the above procedure is not restricted to spheres. Indeed, it applies to other particle shapes as well, provided that the scaling factor $\lambda_{\beta\gamma}$ can be computed. In the case of ellipsoids, this quantity is in fact a direct output of the robust overlap criterion derived by Perram and Wertheim [52]. Combined with our Monte Carlo procedure, this criterion

TABLE I. Generation in four steps of a compact assembly of monodisperse hard spheres. The total number of particles is $N = 4096$, and the final compacity is $f = 0.6375$. In this table, a denotes the particle radius in the current step, f is the effective packing at the end of the current step, ϵ is the numerical parameter governing the cooling schedule (32), and $\mathcal{N}$ is the total number of Monte Carlo cycles in the current step.

Step #	a	f	ϵ	$\mathcal{N}$
1	0.5	0.58	0.01	4082
2	0.51	0.6155	0.005	9269
3	0.5125	0.6246	0.002	18069
4	0.516	0.6375	0.001	44771

allowed the successful generation of compact assemblies of spheroids, an example of which is shown in Fig. 9.

This procedure has been used to generate twenty configurations with increasing polydispersity. Their characteristics are gathered in Table II, where N is the number of globules, L is the size of the (cubic) simulation box, f is the volume fraction of the globules, and α is the polydispersity index, defined as

$$\alpha = \frac{\sqrt{\langle a^2\rangle - \langle a\rangle^2}}{\langle a\rangle}, \quad \langle a\rangle = \frac{1}{N}\sum_{\beta=1}^{N} a_\beta, \quad \langle a^2\rangle = \frac{1}{N}\sum_{\beta=1}^{N} a_\beta^2.$$

As shown in Table II, configurations `monoxxx` are monodisperse (why we considered larger monodisperse configurations; namely `mono020`, `mono024`, `mono028`, and `mono032`, will be explained in Sec. IV B below), while all other configurations are log-normally distributed. After generation, each configuration is scaled so as to ensure that the (number-weighted) average radius $\langle a\rangle$ of the globules is 2.5 nm.

B. Results and discussion

For each value of the polydispersity index α, four configurations were generated. Then, the four (blurred) small-angle scattering spectra were computed according to the procedure described in Sec. III. The average of these four spectra is plotted in Figs. 10 (monodisperse configurations) and 13–15 (polydisperse configurations). In order to allow for the direct comparison of various computations, the scattering intensity is shown in absolute scale in Figs. 10–12, with $\Delta\rho = 1$ nm^{-2}. In Figs. 13–15, arbitrary units are used.

The motivation for averaging four spectra for each value of α is twofold. First, it reduces the statistical noise coming from the insufficient sampling in configurational space. Second, it provides an estimate of this statistical noise (through the point-wise standard deviation of these four spectra). This is represented as error bars in Figs. 10, 13, 14, and 15, and can further be fed into our deconvolution procedure, in order to find

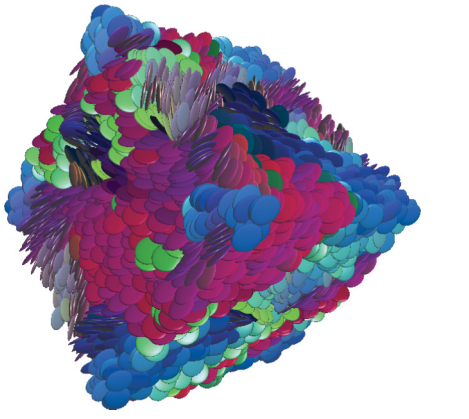

FIG. 9. (Color online) Example of dense packing of oblate spheroids generated following the procedure described in Sec. IV A. The radii of the particles are $a = 200$ (equatorial radius), $c = 25$ (polar radius). The total number of particles is $N = 10\,000$, the compacity is 60%. Each particle is colored according to its orientation, which emphasizes the fact that high compacity causes local orientational order.

TABLE II. Characteristics of the configurations considered in this paper.

Name	N	L [nm]	f	α
`mono004`	4096	75	0.6375	0
`mono008`	4096	75	0.6375	0
`mono012`	4096	75	0.6375	0
`mono016`	4096	75	0.6375	0
`mono020`	32 768	150	0.6375	0
`mono024`	32 768	150	0.6375	0
`mono028`	32 768	150	0.6375	0
`mono032`	32 768	150	0.6375	0
`poly006`	4097	78	0.64	0.20
`poly012`	4097	78	0.64	0.20
`poly018`	4097	78	0.64	0.20
`poly024`	4097	78	0.64	0.20
`poly030`	4094	94	0.64	0.51
`poly036`	4094	94	0.64	0.51
`poly042`	4094	94	0.64	0.51
`poly048`	4094	94	0.64	0.51
`poly051`	4093	115	0.64	0.78
`poly054`	4093	115	0.64	0.78
`poly057`	4093	115	0.64	0.78
`poly060`	4093	115	0.64	0.78

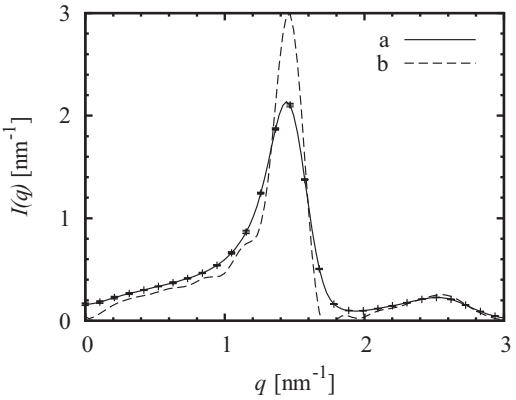

FIG. 10. (a) Average blurred spectrum $I_w(q)$ of configurations `mono004`, `mono008`, `mono012`, `mono016` and (b) resulting deblurred spectrum $I(q)$. In order to allow for the direct comparison of various computations, the scattering intensity is shown in absolute scale in Figs. 10–12, with $\Delta\rho = 1$ nm^{-2}.

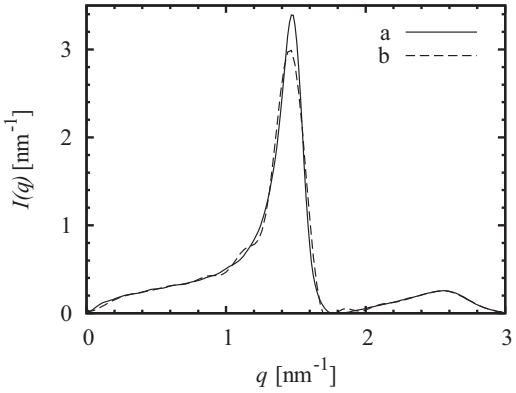

FIG. 11. (a) Deblurred spectrum $I(q)$ of the monodisperse configurations `mono020`, `mono024`, `mono028` and `mono030` and (b) `mono004`, `mono008`, `mono012`, `mono016`. The two graphs are very similar; the location of the peak is identical, while its height is slightly underestimated by the computation on the smaller configurations. This is consistent with the observations made in Sec. III F and confirms the reliability of the proposed method.

the most appropriate value of the regularization parameter λ (see Sec. III E).

The corresponding deblurred spectra $I(q)$ are superimposed with their blurred counterpart $I_w(q)$ in Figs. 10, 13, 14, and 15. Besides, all deblurred spectra are gathered in logarithmic scale in Fig. 17.

We first concentrate on the monodisperse configurations, `mono004`, `mono008`, `mono012`, and `mono016`, whose average scattering pattern (see Fig. 10) exhibits a sharp peak. This indicates pseudoperiodicity in the real space, which was to be expected, as the unique diameter $d = 5$ nm of the particles constitutes such a pseudoperiod (d is also the minimum center-to-center distance). Interestingly however, our calculation shows that the actual location of the peak ($q_{\text{peak}} \simeq 1.47$ nm^{-1}) is greater than $2\pi/d = 1.25$ nm^{-1}, in good agreement with results published elsewhere [34].

Another remarkable feature of Fig. 10 is the behavior of $I(q)$ as $q \to 0$. Indeed, it seems that $I(0) \simeq 0$. In order to confirm this result, the same computation was carried out

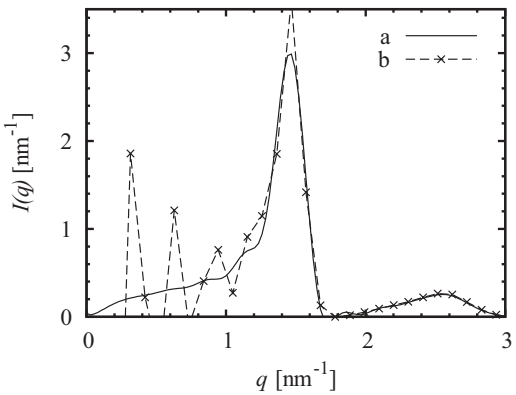

FIG. 12. Average scattering intensity $I(q)$ of the monodisperse configurations `mono004`, `mono008`, `mono012`, `mono016` computed with (a) the procedure proposed in this paper and (b) the procedure of Salacuse *et al.* [12,32]. The latter is more sensitive than the former to ensemble size effects.

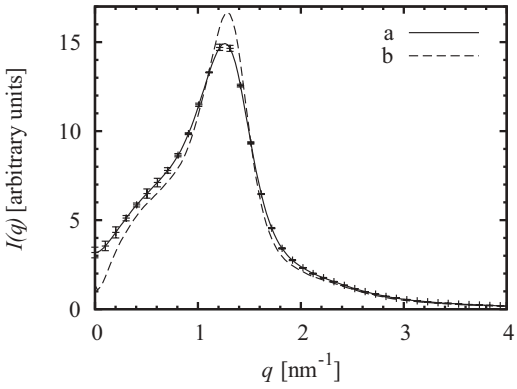

FIG. 13. (a) Average blurred spectrum $I_w(q)$ of configurations `poly006`, `poly012`, `poly018`, `poly024` ($\alpha = 0.20$) and (b) resulting deblurred spectrum $I(q)$.

on simulation boxes twice as large (configurations `mono020`, `mono024`, `mono028`, and `mono030`, see Table II). The resulting deblurred spectrum is shown in Fig. 11, where it is again observed that $I(0) \simeq 0$. This result should therefore not be considered as a size effect, but as a general feature of systems approaching the random close-packing density, which are almost incompressible. It should be noted that the same observation was made by Donev *et al.* [34] using different numerical means, with much larger assemblies of spheres (more than a million particles); this confirms the robustness of the method presented in Sec. III.

To close our analysis of the monodisperse configurations, Fig. 12 shows a comparison between two procedures for the computation of the scattering intensity. Curve (a) results from the application of our procedure, while curve (b) results from the application of the procedure proposed by Salacuse *et al.* [12,32]. In both cases, the corrections for anomalous size effects are similar. Therefore, the oscillations observed in (b) should be attributed to ensemble size effects. Indeed, only four configurations are considered for this computation, which is clearly insufficient in the approach of Salacuse *et al.* These oscillations are not observed in (a), because sampling is widened in this case by the introduction of several windows. Due to the fact that the *same* configuration may be

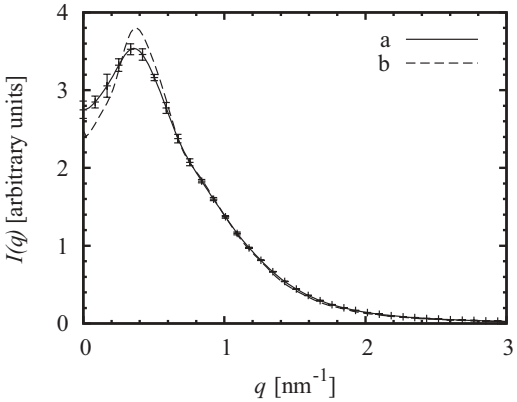

FIG. 14. (a) Average blurred spectrum $I_w(q)$ of configurations `poly030`, `poly036`, `poly042`, `poly048` ($\alpha = 0.51$) and (b) resulting deblurred spectrum $I(q)$.

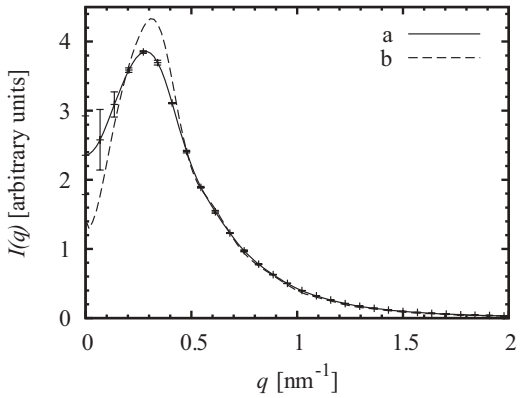

FIG. 15. (a) Average blurred spectrum $I_w(q)$ of configurations poly051, poly054, poly057, poly060 ($\alpha = 0.78$) and (b) resulting deblurred spectrum $I(q)$.

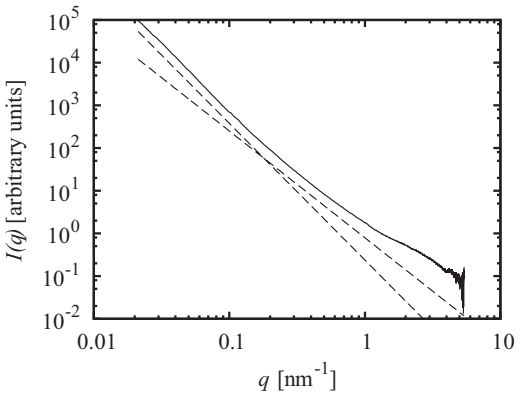

FIG. 16. SAXS data for a 1.5 year old CEM-I cement paste ($w/c = 0.35$). Dashed lines represent the algebraic branches $q^{-3.2}$ and $q^{-2.5}$. This data will serve as a reference to all subsequent numerical simulations.

observed multiple times (albeit through different windows), this sampling is *biased*, and results in expression (13), rather than the straightforward $I_w(q) = I(q)$.

We now turn to the polydisperse configurations (Figs. 13–15). Similarly to the monodisperse case, each spectrum is strongly peaked around a rather small value ($0.05\ \text{nm}^{-1} \leqslant q_{\text{peak}} \leqslant 1.5\ \text{nm}^{-1}$). This again indicates pseudoperiodicity in the real space, which is due to the high compacity of the systems we generated. We note that the location q_{peak} of this peak shifts towards the origin ($q = 0$) as the polydispersity index α increases. We were not able, however, to relate the location of the peak, q_{peak}, to the average radius of the particles through a simple law such as $q_{\text{peak}}\langle a\rangle \sim$ const.; therefore, the physical interpretation of the characteristic length scale to which q_{peak} relates remains unclear. We also note that this peak tends to widen as the polydispersity index α increases; this suggests that it would ultimately vanish for very high polydispersity.

Finally, similarly to the monodisperse case, it is possible to compare our procedure to the procedure of Lajovic *et al.* [29]. The results are not presented here, because they are similar to Fig. 12. This means that, when the compacity increases, the procedure of Lajovic *et al.* [29] becomes increasingly sensitive to size effects, while ours remains more robust against these effects. This result was somewhat expected from the analysis shown in Fig. 12, since the procedure of Lajovic *et al.* [29] coincides with the procedure of Salacuse *et al.* [12] in the monodisperse case.

V. PERSPECTIVES: APPLICATION TO CEMENT PASTES

Investigation of cement pastes by small-angle scattering started in the mid eighties [13,53,54]. Since then, it never failed to generate interest, as suggested by the large number of publications reporting on this subject [13,14,53–65]. One of the reasons for this keen interest is the fact that, regardless of the precise composition or the age of the hardened cement paste, the scattering intensity $I(q)$ invariably behaves as a fractional power of q over a wide range of this parameter.

Figure 16 is a typical example of the intensity scattered by a cement paste. In the present case, the specimen was made from CEM-I cement, cast in a cylindrical mold (70 mm × 140 mm), where it stayed for a year; the water-to-cement ratio was $w/c = 0.35$. The mold was then unsealed, and the specimen was wrapped in two layers of aluminum foil and stored at room temperature for six months; this sample preparation is routinely invoked at the Institut français des sciences et technologies des transports, de l'aménagement et des réseaux (IFSTTAR) [66] in order to maintain endogenous conditions. This sample (previously cut in 0.1-mm-thick slices, and stored in water) was then submitted to small-angle x-ray scattering at the synchrotron Soleil (beamline Swing). The wavelength of the x-rays was 0.127 nm, and the sample-to-detector distance was successively 1.50 m then 6 m.

The resulting spectrum (see Fig. 16) clearly shows the existence of two power-law regimes, with a transition around $q \simeq 0.2\ \text{nm}^{-1}$:

$$I(q) \propto \begin{cases} q^{-(3+\epsilon_s)} & \text{for} \quad q \leqslant 0.2\ \text{nm}^{-1} \\ q^{-(2+\epsilon_v)} & \text{for} \quad q \geqslant 0.2\ \text{nm}^{-1}, \end{cases}$$

with $\epsilon_s \simeq 0.2$ and $\epsilon_v \simeq 0.5$, which is in good agreement with many other published results [14,53,55,58,59,67,68].

As stated in Sec. I, the popular globular model of cement describes C–S–H as an assembly of near-spherical, densely packed particles, with a porosity around 0.30–0.35 [15]. Figure 10 [see also Fig. 17(a)] shows that the scattering intensity $I(q)$ of such monodisperse configurations behaves as q^{-4} (the so-called *Porod regime*) at high q, exhibits a strong correlation peak at $q \simeq 2\pi/d$, and ends in a pseudoplateau with a negative slope at low q. Obviously, such a pattern does not fit the experimental data (Fig. 16), and the globular model must be revised.

A first option would be to consider a set of monodisperse discotic colloids (see Fig. 9). This would lead to $I(q)$ behaving as q^{-2} at high q, in closer agreement with the experimental data. As shown in Fig. 9, however, for dense disordered packings, "colonar" order is observed on the length scale of a few particle diameters. At larger length scales, the system therefore reaches statistical homogeneity. In other words, similarly to assemblies of spherical particles, $I(q)$ must exhibit a plateau at low q, which is confirmed by computations not presented here. Such a plateau is not observed experimentally.

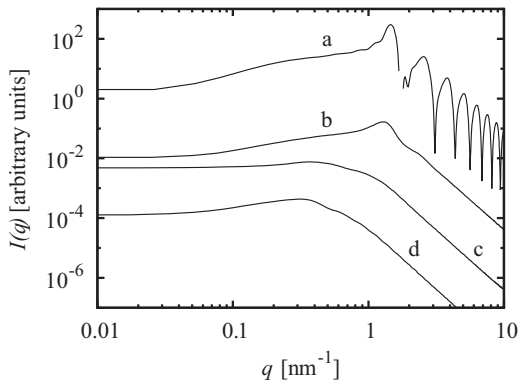

FIG. 17. Computed scattering intensity of configurations (a) $\alpha = 0$, (b) $\alpha = 0.20$, (c) $\alpha = 0.51$, and (d) $\alpha = 0.78$. It should be noted that small-angle scattering spectra are generally known up to an arbitrary multiplicative constant (arbitrary translation along the vertical axis, in the logarithmic scale). Therefore, the four curves presented here were spread vertically in order to improve legibility.

A second option would be to consider interactions between particles. Obviously, attractive interactions between elementary particles must exist in cement pastes. Diffusion- and reaction-limited aggregation (DLCA and RLCA) processes are simple examples which are known to lead to mass fractal structures, the scattering intensity of which behaves as $q^{-\nu}$ [1,69,70]. However, these structures are relatively open and cannot account for the low porosity of C–S–H. Besides, applicability of DLCA and RLCA to the hydration of cement pastes is highly doubtful; packing-limited growth processes [71] would probably be more appropriate.

A third option is explored in the present work, where particle polydispersity is introduced. In the remainder of this section, the ability of the configurations considered in Sec. IV to describe C–S–H is discussed. These assemblies of spheres share the same compacity $f \simeq 0.64$, which is representative of C–S–H in cement pastes [15], while their polydispersity index varies. All computed spectra (see Figs. 10 to 15) have been gathered in Fig. 17, where a logarithmic scale has been adopted. It should be recalled that, after generation, each configuration is scaled so as to ensure that the (number-weighted) average radius $\langle a \rangle$ of the globules is 2.5 nm (consistent with the globular model of C–S–H): all spectra therefore share the same reference length scale, and direct comparison is meaningful.

Observation of Fig. 17 shows that, in all instances, the beginning of the Porod regime [$I(q) \propto q^{-4}$] follows closely the correlation peak, leaving virtually no space for an alternative power law to develop. It is also observed that in the low-q range, the spectra quickly reach a plateau. The computed spectra therefore share no common feature with the experimental intensity scattered by cement pastes. In other words, none of the systems considered in Sec. IV can be regarded as convincing models of calcium-silicate hydrates in cement pastes.

One of the most remarkable features shared by all curves shown in Figs. 10 to 15 is the existence of a marked correlation peak. This peak tends to spread when the polydispersity index α increases, which suggests that we should consider a system with a very wide particle-size distribution. Widening this distribution tends to increase significantly the number of particles in numerical simulations. For this reason, we had to give up the generation of a random medium, and chose an Apollonius packing of spheres instead (see Fig. 18).

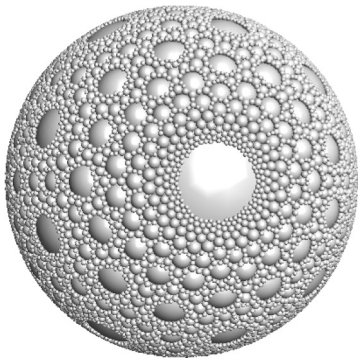

FIG. 18. Three-dimensional view of apollonian packing of spheres.

The particle size distribution of the Apollonius packing is $N(a) \propto a^{-d_v-1}$, where $N(a)da$ denotes the total number of spheres with radius between a and $a + da$, and $d_v \simeq 2.47$ denotes the fractal dimension [72]. More details on the generation of the packing, as well as the computation of its small-angle scattering spectrum can be found in Appendix E.

The resulting scattering intensity curve is shown in Fig. 19, where it is compared to an approximate calculation based on the chord-length distributions [[73], Eq. (40)]:

$$I(q) \simeq -\frac{\pi \Delta\rho^2 S_v}{q} \frac{d}{dq} \left\{ \frac{1}{q^2} \mathrm{Real}\left(\frac{[1 - \hat{f}_s(q)][1 - \hat{f}_p(q)]}{1 - \hat{f}_s(q)\hat{f}_p(q)} \right) \right\}, \tag{33}$$

where S_v is the specific surface, f_s (f_p) is the probability density function of μ chords measured in the solid (the pores), and $\hat{f}_s$ ($\hat{f}_p$) its Fourier transform. The above approximate formula is valid, provided that the length of successive chords measured along the same random line are uncorrelated [73]. While this assumption would not be verified for the mildly polydisperse configurations considered in Sec. IV, it is acceptable for highly polydisperse configurations, and our method is indeed in good agreement with Eq. (33) (see Fig. 19).

Observation of Fig. 19 shows that the scattering intensity curve comprises two power-law branches with a transition at $q a_{\min} \simeq \pi$ ($a_{\min}$ is the radius of the smallest particles). At high q, the Porod regime $I(q) \propto q^{-4}$ is retrieved, while at low q, the fractional power law $I(q) \propto q^{-2.47}$ is observed. The latter regime is consistent with the dimension $d_v \simeq 2.47$ of the apollonian packing, which is a mass fractal [72], for which the scattered intensity must behave as q^{-d_v} [74–76].

Because of the absence of a correlation peak, the spectrum shown in Fig. 19 is much more satisfactory than all other spectra shown in Fig. 17, even if the exponent of the power law does not match the values generally observed for cement pastes, and the resulting spectrum is therefore not fully consistent with experimental data.

The present calculation is encouraging because it suggests that the scattering intensity of packings with carefully chosen power-law size distributions might exhibit the two features: absence of correlation peak and existence of power-law branches (other than the classical Porod regime), which are

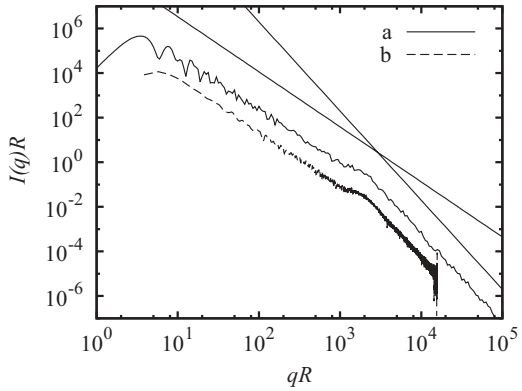

FIG. 19. Scattered intensity pattern of the Apollonius packing shown in Fig. 18, computed (a) with the method proposed in this paper and (b) with the approximate formula (33). The two curves are in excellent agreement and match perfectly without rescaling. For the sake of readability, curve (b) has been translated vertically. The two straight lines represent the expected fractal [$I(q) \propto q^{-2.47}$, low q] and Porod [$I(q) \propto q^{-4}$, high q] regimes. In order to allow for the direct comparison of the two methods, both q and $I(q)$ have been made dimensionless through multiplication by the external radius R of the packing; furthermore, $\Delta\rho = 10^{10} R^{-2}$.

required to provide a convincing microstructural model of cement pastes.

To close this section, it should be noted that, due to its $O(N^2)$ complexity, the computation of the scattering intensity with the method of Lajovic *et al.* [29] would have been very difficult; indeed, on a standard laptop, the estimated required time was about 2200 days, while our computation, which has $O(N)$ complexity, ran in only 2 days on the same computer.

VI. CONCLUSION

In this paper, we proposed a new method for the computation of the scattering intensity of computer-generated microstructures. Although generally more CPU intensive than previously proposed methods for medium-sized configurations, it is more accurate at low q and more robust with respect to ensemble size effects, particularly with dense configurations. It is also highly efficient in special situations where the spectrum must be updated following small alterations of the microstructure, or for very large configurations.

This method was validated against simple simulations and subsequently applied to dense polydisperse distributions of hard spheres, for which a new generation procedure was also introduced.

Analysis of these computations shows that if the particle size distribution is too narrow, the small-angle scattering spectrum exhibits a sharp correlation peak, and no power-law regime (other than the Porod regime). Such microstructures are therefore not representative of hardened cement pastes.

By contrast, the correlation peak vanishes as the particle size distribution widens. Moreover, if the distribution follows a power law, then the scattering intensity also follows a power law.

This might suggest that the sizes of the C–S–H globules in hardened cement pastes are distributed according to a power law. We find this conclusion questionable, since such a distribution would lead to very wide polydispersity, which very few—if any—known elaboration processes could explain convincingly. Owing to Babinet's principle, a dual hypothesis would be to assume that the sizes of the *pores* are distributed according to a power law. This assumption will be explored in future work.

Even if their applicability to cementitious materials is questionable, dense assemblies of polydisperse particles with a power-law size distribution are interesting models. The apollonian packing is a realization of such a system; however, the corresponding exponent of q in the small-angle scattering spectrum is not tunable. We therefore aim at developing a procedure for the generation of random configurations with tunable powers and relate this power to that of the scattering intensity curve.

APPENDIX A: RELATIONSHIP BETWEEN REAL AND BLURRED SPECTRA

In the present section, identity (13) is proved under the assumption that the unit cell $\mathcal{U}$ is cubic, with sides of length L. Extension to unit cells with unequal sides is straightforward. All simulations being carried out within the framework of the minimum image convention [42], the fluctuations η of the scattering-length density can be decomposed in a Fourier series

$$\eta(\boldsymbol{x}) = \sum_{\boldsymbol{n}\in\mathbb{Z}^3} \hat{\eta}_{\boldsymbol{n}} \exp(i\boldsymbol{k}_{\boldsymbol{n}} \cdot \boldsymbol{x}), \tag{A1}$$

where $\boldsymbol{k}_{\boldsymbol{n}} = (2\pi/L)\boldsymbol{n}$, and $\hat{\eta}_{\boldsymbol{n}}$ is the discrete Fourier transform

$$\hat{\eta}_{\boldsymbol{n}} = \frac{1}{|\mathcal{U}|} \int_{\boldsymbol{x}\in\mathcal{U}} \eta(\boldsymbol{x}) \exp(-i\boldsymbol{k}_{\boldsymbol{n}} \cdot \boldsymbol{x}) d^3\boldsymbol{x}.$$

Substituting (A1) in Eq. (11), we find

$$A_{\mathrm{w}}(\boldsymbol{q},\boldsymbol{x}) = \sum_{\boldsymbol{n}\in\mathbb{Z}^3} \hat{\eta}_{\boldsymbol{n}} \hat{w}(\boldsymbol{q} - \boldsymbol{k}_{\boldsymbol{n}}) \exp[-i(\boldsymbol{q} - \boldsymbol{k}_{\boldsymbol{n}}) \cdot \boldsymbol{x}], \tag{A2}$$

where the continuous Fourier transform $\hat{w}$ of the characteristic function of the window $\mathcal{W}$ has been introduced

$$\hat{w}(\boldsymbol{k}) = \int_{\boldsymbol{x}\in\mathbb{R}^3} w(\boldsymbol{x}) \exp(-i\boldsymbol{k} \cdot \boldsymbol{x}) d^3\boldsymbol{x}.$$

Then, by definition (12), the blurred spectrum $I_{\mathrm{w}}(\boldsymbol{q})$ is the volume average of the squared modulus of A_{w}. Using Eq. (A2),

$$|A_{\mathrm{w}}(\boldsymbol{q},\boldsymbol{x})|^2 = \sum_{\boldsymbol{m},\boldsymbol{n}\in\mathbb{Z}^3} \hat{\eta}^*_{\boldsymbol{m}} \hat{\eta}_{\boldsymbol{n}} \hat{w}(\boldsymbol{q} - \boldsymbol{k}_{\boldsymbol{m}}) \hat{w}^*(\boldsymbol{q} - \boldsymbol{k}_{\boldsymbol{n}}) \times \exp[-i(\boldsymbol{k}_{\boldsymbol{n}} - \boldsymbol{k}_{\boldsymbol{m}}) \cdot \boldsymbol{x}].$$

Upon integration on the unit cell $\mathcal{U}$, the terms with $\boldsymbol{m} \neq \boldsymbol{n}$ vanish, and

$$I_{\mathrm{w}}(\boldsymbol{q}) = \frac{1}{|\mathcal{W}|} \sum_{\boldsymbol{n}\in\mathbb{Z}^3} |\hat{\eta}_{\boldsymbol{n}}|^2 |\hat{w}(\boldsymbol{q} - \boldsymbol{k}_{\boldsymbol{n}})|^2. \tag{A3}$$

We now introduce the normalized correlation function $\gamma_{\mathrm{w}}(\boldsymbol{r})$ of the window $\mathcal{W}$, as well as its continuous Fourier

transform $\hat{\gamma}_{\mathrm{w}}(\boldsymbol{k})$:

$$\gamma_{\mathrm{w}}(\boldsymbol{r}) = \frac{1}{|\mathcal{W}|}\int_{\boldsymbol{x}\in\mathbb{R}^3} w(\boldsymbol{x})w(\boldsymbol{x}+\boldsymbol{r})d^3\boldsymbol{x}, \tag{A4}$$

$$\hat{\gamma}_{\mathrm{w}}(\boldsymbol{k}) = \int_{\boldsymbol{r}\in\mathbb{R}^3} \gamma_{\mathrm{w}}(\boldsymbol{r})\exp(-i\boldsymbol{k}\cdot\boldsymbol{r})d^3\boldsymbol{r}. \tag{A5}$$

From the convolution theorem, we have $\hat{\gamma}_{\mathrm{w}}(\boldsymbol{k}) = |\mathcal{W}|^{-1}|\hat{w}(\boldsymbol{k})|^2$ and Eq. (A3) can be rewritten as

$$\begin{aligned} I_{\mathrm{w}}(\boldsymbol{q}) &= \sum_{\boldsymbol{n}\in\mathbb{Z}^3} |\hat{\eta}_{\boldsymbol{n}}|^2 \hat{\gamma}_{\mathrm{w}}(\boldsymbol{q}-\boldsymbol{k}_n) \\ &= \int_{\boldsymbol{r}\in\mathbb{R}^3} \left[\sum_{\boldsymbol{n}\in\mathbb{Z}^3} |\hat{\eta}_{\boldsymbol{n}}|^2 \exp(i\boldsymbol{k}_{\boldsymbol{n}}\cdot\boldsymbol{r})\right] \\ &\quad \times \gamma_{\mathrm{w}}(\boldsymbol{r})\exp(-i\boldsymbol{q}\cdot\boldsymbol{r})d^3\boldsymbol{r}. \end{aligned} \tag{A6}$$

The quantity inside the square brackets is the autocorrelation of the fluctuations of the scattering-length density, which is defined by analogy with Eq. (5) (where the ensemble average $\langle\eta^2\rangle$ is replaced by the volume average $\overline{\eta^2}$):

$$\gamma(\boldsymbol{r};\mathcal{U}) = \frac{1}{\overline{\eta^2}}\frac{1}{|\mathcal{U}|}\int_{\boldsymbol{x}\in\mathcal{U}} \eta(\boldsymbol{x})\eta(\boldsymbol{x}+\boldsymbol{r})d^3\boldsymbol{x},$$

where the notation $\gamma(\boldsymbol{r};\mathcal{U})$ instead of $\gamma(\boldsymbol{r})$ is a reminder of the fact that the above autocorrelation is computed on a finite size simulation box and therefore differs from the true autocorrelation of the random medium under consideration.

Obviously, $\gamma(\boldsymbol{r};\mathcal{U})$ has the same (L,L,L) periodicity as η and can also be decomposed in a Fourier series. Furthermore, from the convolution theorem

$$\gamma(\boldsymbol{r};\mathcal{U}) = \frac{1}{\overline{\eta^2}}\sum_{\boldsymbol{n}\in\mathbb{Z}^3} |\hat{\eta}_{\boldsymbol{n}}|^2 \exp(i\boldsymbol{k}_{\boldsymbol{n}}\cdot\boldsymbol{r}).$$

Combining with Eq. (A6), we find that

$$I_{\mathrm{w}}(\boldsymbol{q}) = \overline{\eta^2}\int_{\boldsymbol{r}\in\mathbb{R}^3} \gamma(\boldsymbol{r};\mathcal{U})\gamma_{\mathrm{w}}(\boldsymbol{r})\exp(-i\boldsymbol{q}\cdot\boldsymbol{r})d^3\boldsymbol{r}.$$

If the unit cell $\mathcal{U}$ is large enough, then for $|\boldsymbol{r}| < L/2$, we have $\gamma(\boldsymbol{r};\mathcal{U}) = \gamma(\boldsymbol{r})$, where $\gamma(\boldsymbol{r})$ denotes the true autocorrelation (of infinitely large samples). Also, if $|\boldsymbol{r}| > \mathrm{diam}\mathcal{W}$ (diameter of the window), then $\gamma_{\mathrm{w}}(\boldsymbol{r}) = 0$. Therefore, provided the diameter of the window is not greater than half the size of the unit cell, we have for all $\boldsymbol{r}\in\mathbb{R}^3$

$$\gamma(\boldsymbol{r};\mathcal{U})\gamma_{\mathrm{w}}(\boldsymbol{r}) = \gamma(\boldsymbol{r})\gamma_{\mathrm{w}}(\boldsymbol{r}),$$

and

$$I_{\mathrm{w}}(\boldsymbol{q}) = \overline{\eta^2}\int_{\boldsymbol{r}\in\mathbb{R}^3} \gamma(\boldsymbol{r})\gamma_{\mathrm{w}}(\boldsymbol{r})\exp(-i\boldsymbol{q}\cdot\boldsymbol{r})d^3\boldsymbol{r}.$$

Unlike $\gamma(\boldsymbol{r};\mathcal{U})$ (which is periodic), $\gamma(\boldsymbol{r})$ can be Fourier transformed (under the no long-range order assumption). Invoking again the convolution theorem, we finally find

$$I_{\mathrm{w}}(\boldsymbol{q}) = \frac{1}{(2\pi)^3}\int_{\boldsymbol{p}\in\mathbb{R}^3} \hat{\gamma}_{\mathrm{w}}(\boldsymbol{q}-\boldsymbol{p})\overline{\eta^2}\hat{\gamma}(\boldsymbol{p})d^3\boldsymbol{p}.$$

For sufficiently large simulation boxes, $\overline{\eta^2} = \langle\eta^2\rangle$, and comparison with Eq. (4) shows that $\overline{\eta^2}\hat{\gamma}(\boldsymbol{q})$ is indeed the scattered intensity $I(\boldsymbol{q})$. Therefore, identity (13) is retrieved.

APPENDIX B: ISOTROPIC AVERAGE OF BLURRED SPECTRUM

In this section we give a proof of identity (17). Combining Eqs. (13) and (16), the following integral must be simplified:

$$I_{\mathrm{w}}(q) = \frac{1}{32\pi^4}\int_{|\boldsymbol{n}|=1}\int_{\boldsymbol{p}\in\mathbb{R}^3} \hat{\gamma}_{\mathrm{w}}(q\boldsymbol{n}-\boldsymbol{p})I(\boldsymbol{p})d^3\boldsymbol{p}d^2\boldsymbol{n}. \tag{B1}$$

We first concentrate on the integration with respect to the unit vector $\boldsymbol{n}$. From Eq. (A5)

$$\begin{aligned} \int_{|\boldsymbol{n}|=1} \hat{\gamma}_{\mathrm{w}}(q\boldsymbol{n}-\boldsymbol{p})d^2\boldsymbol{n} &= \int_{\boldsymbol{r}\in\mathbb{R}^3} \gamma_{\mathrm{w}}(\boldsymbol{r})\exp(i\boldsymbol{p}\cdot\boldsymbol{r}) \\ &\quad \times \int_{|\boldsymbol{n}|=1} \exp(-iq\boldsymbol{n}\cdot\boldsymbol{r})d^2\boldsymbol{n}d^3\boldsymbol{r}. \end{aligned} \tag{B2}$$

Using the known identity

$$\frac{1}{4\pi}\int_{|\boldsymbol{n}|=1} \exp(-i\boldsymbol{z}\cdot\boldsymbol{n})d^2\boldsymbol{n} = \mathrm{sinc}|\boldsymbol{z}|, \tag{B3}$$

Eq. (B2) reduces to

$$\begin{aligned} &\frac{1}{4\pi}\int_{|\boldsymbol{n}|=1} \hat{\gamma}_{\mathrm{w}}(q\boldsymbol{n}-\boldsymbol{p})d^2\boldsymbol{n} \\ &\quad = \int_{\boldsymbol{r}\in\mathbb{R}^3} \gamma_{\mathrm{w}}(\boldsymbol{r})\exp(i\boldsymbol{p}\cdot\boldsymbol{r})\mathrm{sinc}(qr)d^3\boldsymbol{r}. \end{aligned}$$

Since the window $\mathcal{W}$ is spherical, $\gamma_{\mathrm{w}}(\boldsymbol{r})$ is a function of the norm r of $\boldsymbol{r}$ only, and integration in spherical coordinates with respect to $\boldsymbol{r}$ leads to

$$\begin{aligned} &\frac{1}{4\pi}\int_{|\boldsymbol{n}|=1} \hat{\gamma}_{\mathrm{w}}(q\boldsymbol{n}-\boldsymbol{p})d^2\boldsymbol{n} \\ &\quad = \int_0^{+\infty}\int_{|\boldsymbol{n}|=1} \exp(ir\boldsymbol{p}\cdot\boldsymbol{n})d^2\boldsymbol{n}\gamma_{\mathrm{w}}(r)\mathrm{sinc}(qr)r^2dr \\ &\quad = \int_0^{+\infty} 4\pi r^2\gamma_{\mathrm{w}}(r)\mathrm{sinc}(pr)\mathrm{sinc}(qr)dr, \end{aligned}$$

where Eq. (B3) has again been used. Substitution into Eq. (B1) gives

$$\begin{aligned} I_{\mathrm{w}}(q) &= \frac{1}{(2\pi)^3}\int_{\boldsymbol{p}\in\mathbb{R}^3} I(\boldsymbol{p})\int_{r\geqslant 0} 4\pi r^2\gamma_{\mathrm{w}}(r) \\ &\quad \times \mathrm{sinc}(pr)\mathrm{sinc}(qr)drd^3\boldsymbol{p}. \end{aligned}$$

Integration with respect to $\boldsymbol{p}$ is again performed in spherical coordinates ($\boldsymbol{p} = p\boldsymbol{n}$, $|\boldsymbol{n}| = 1$):

$$\begin{aligned} I_{\mathrm{w}}(q) &= \frac{2}{\pi}\int_{p\geqslant 0}\int_{r\geqslant 0}\left[\frac{1}{4\pi}\int_{|\boldsymbol{n}|=1} I(p\boldsymbol{n})d^2\boldsymbol{n}\right]r^2\gamma_{\mathrm{w}}(r) \\ &\quad \times \frac{\sin(pr)}{pr}\frac{\sin(qr)}{qr}drp^2dp, \end{aligned}$$

where the term in square brackets is the isotropic average $I(q)$ of the true spectrum $I(\boldsymbol{q})$, and the above expression reduces to

$$\begin{aligned} qI_{\mathrm{w}}(q) &= \frac{2}{\pi}\int_{p\geqslant 0}\int_{r\geqslant 0} pI(p)\gamma_{\mathrm{w}}(r) \\ &\quad \times \sin(pr)\sin(qr)drdp. \end{aligned} \tag{B4}$$

For spherical windows, $\gamma_w(r) = 0$ when $r \geqslant 2R$. When $r \leqslant 2R$, $\gamma_w(r)$ is given by [see, e.g., Ref. [77], Eq. (3.51)]

$$\gamma_w(r) = 1 - \frac{3}{4}\frac{r}{R} + \frac{1}{16}\left(\frac{r}{R}\right)^3 \quad (r \leqslant 2R),$$

which is substituted into Eq. (B4):

$$qI_w(q) = \frac{2R}{\pi}\int_{p\geqslant 0} pI(p)\int_{x=0}^{x=2}\left(1 - \frac{3}{4}x + \frac{1}{16}x^3\right) \times \sin(pRx)\sin(qRx)dxdp.$$

Simple algebra finally shows that the above expression coincides with Eq. (17).

APPENDIX C: PARTIAL FORM FACTOR OF SPHERICAL PARTICLES

In this section, we propose a numerical method for the computation of the integral in Eq. (19); namely,

$$G(\boldsymbol{q},\boldsymbol{x}) = \int_{\boldsymbol{y}\in\omega} w(\boldsymbol{y}-\boldsymbol{x})\exp(-i\boldsymbol{q}\cdot\boldsymbol{y})d^3\boldsymbol{y}, \qquad \text{(C1)}$$

when the particle ω is partially included in the window $\mathcal{W}$, both being spherical. The spherical window $\mathcal{W}$ is centered at $\boldsymbol{x}$, while the spherical particle is centered at $\boldsymbol{x} + r\boldsymbol{n}$ ($|\boldsymbol{n}| = 1$). Then $G(\boldsymbol{q},\boldsymbol{x})$ reads

$$G(\boldsymbol{q},\boldsymbol{x}) = \exp(-i\boldsymbol{q}\cdot\boldsymbol{x})\int_{\substack{|z|\leqslant R\\ |z-r\boldsymbol{n}|\leqslant a}} \exp(-i\boldsymbol{q}\cdot\boldsymbol{z})d^3\boldsymbol{z},$$

where R (a) denotes the radius of the spherical window (the spherical particle). Since the particle is partially included in the window, we have $R - a \leqslant r \leqslant R + a$. The above integral is best computed in cylindrical coordinates $\boldsymbol{z} = \rho\cos\theta\boldsymbol{e}_1 + \rho\sin\theta\boldsymbol{e}_2 + \zeta\boldsymbol{e}_3$, with

$$\boldsymbol{e}_3 = \boldsymbol{n}, \quad \boldsymbol{e}_2 = \frac{\boldsymbol{n}\wedge\boldsymbol{q}}{|\boldsymbol{n}\wedge\boldsymbol{q}|}, \quad \boldsymbol{e}_1 = \boldsymbol{e}_2\wedge\boldsymbol{e}_3.$$

In this set of axes, $\boldsymbol{q}$ has no component along $\boldsymbol{e}_2$:

$$\boldsymbol{q} = q_\perp\boldsymbol{e}_1 + q_\parallel\boldsymbol{e}_3, \quad q_\parallel = \boldsymbol{q}\cdot\boldsymbol{n}, \quad q_\perp = \sqrt{q^2 - q_\parallel^2},$$

while the joint conditions $|\boldsymbol{z}| \leqslant R$ and $|\boldsymbol{z} - r\boldsymbol{n}| \leqslant a$ reduce to $\rho \leqslant \rho_{\max}(\zeta)$, with

$$\rho_{\max}(\zeta)^2 = \begin{cases} a^2 - (\zeta - r)^2 & \text{if} \quad r - a \leqslant \zeta \leqslant \zeta^* \\ R^2 - \zeta^2 & \text{if} \quad \zeta^* \leqslant \zeta \leqslant R, \end{cases}$$

where $\zeta^* = (R^2 + r^2 - a^2)/(2r)$. Combining the above equalities leads to the following expression:

$$G(\boldsymbol{q},\boldsymbol{x}) = \exp(-i\boldsymbol{q}\cdot\boldsymbol{x})\int_{r-a}^{R}\int_0^{\rho_{\max}(\zeta)} \times \int_0^{2\pi}\rho\exp[-i(q_\perp\rho\cos\theta + q_\parallel\zeta)]d\theta d\rho d\zeta.$$

A closed-form expression for the integral with respect to θ can be found in, e.g., Ref. [78], 9.1.18:

$$G(\boldsymbol{q},\boldsymbol{x}) = 2\pi\exp(-i\boldsymbol{q}\cdot\boldsymbol{x}) \times \int_{r-a}^{R}\int_0^{\rho_{\max}(\zeta)}\rho J_0(k_\perp\rho)\exp(-iq_\parallel\zeta)d\rho d\zeta,$$

where J_k is the Bessel function of kth order and first kind. Similarly, integration with respect to ρ can be performed analytically (see, e.g., Ref. [79], 5.52):

$$G(\boldsymbol{q},\boldsymbol{x}) = \frac{2\pi}{k_\perp^2}\exp(-i\boldsymbol{q}\cdot\boldsymbol{x})\int_{r-a}^{R} q_\perp\rho_{\max}(\zeta)J_1[q_\perp\rho_{\max}(\zeta)] \times \exp(-iq_\parallel\zeta)d\zeta.$$

The above formula shows that the volume integral (C1) reduces to a single integral, which is computed numerically. The interval of integration is decomposed into subintervals delimited by the roots of the oscillatory integrand. On each of the subintervals, standard Gauss-Legendre quadrature (with typically 10 to 15 Gauss points) is used. It should be noted that to increase the efficiency of this scheme, approximate formulas provided by Abramowitz and Stegun [[78], 9.4.4 and 9.4.6]] are used for J_1.

APPENDIX D: FOURIER TRANSFORM OF CONVOLUTION KERNEL

The Fourier transform $\hat{k}(x)$ of the convolution kernel $k(q)$, defined by Eqs. (18) and (21), is given by the following two relations:

$$\hat{k}(x) = \frac{3}{\pi}\hat{\varphi}\left(\frac{x}{2R}\right), \qquad \text{(D1)}$$

$$\hat{\varphi}(\omega) = \begin{cases} 0 & \text{if} \quad |\omega| \geqslant 1 \\ \frac{1}{3}\pi\left(1 + \frac{3}{2}\omega - \frac{1}{2}\omega^3\right) & \text{if} \quad -1 \leqslant \omega \leqslant 0 \\ \frac{1}{3}\pi\left(1 - \frac{3}{2}\omega + \frac{1}{2}\omega^3\right) & \text{if} \quad 0 \leqslant \omega \leqslant 1, \end{cases} \qquad \text{(D2)}$$

where it is noted that Eq. (D2) is readily derived from the definition of the Fourier transform $\hat{\varphi}$ of φ

$$\hat{\varphi}(\omega) = \int_{-\infty}^{+\infty}\varphi(t)e^{-i\omega t}dt,$$

as well as the standard formula (to be understood in the sense of generalized functions)

$$\int_{-\infty}^{+\infty}\frac{e^{-i\omega t}}{t^n}dt = -i\pi\frac{(-i\omega)^{n-1}}{(n-1)!}\mathrm{sgn}(\omega).$$

Substitution in Eq. (D1) provides a closed-form expression for $\hat{k}(x)$, from which it is apparent that $\hat{k}(x) = 0$ for $|x| \geqslant 2R$.

APPENDIX E: GENERATION OF APOLLONIAN PACKING AND COMPUTATION OF SCATTERING INTENSITY

The generation of the configuration proceeds according to the efficient method outlined in Ref. [72]. The external radius of the packing is $R = 1.0$, and the radius of the largest spheres is $a_{\max} \simeq 0.7R$. All spheres with a radius greater than $a_{\min} = 10^{-3}R$ were generated; this led to an assembly of $N = 5\,974\,835$ spheres.

Because the configuration at hand was not a realization of a random medium, the method described in Sec. III had to

be adapted in order to allow the computation of the small-angle scattering spectrum of the apollonian packing. More precisely, in the general method presented above, statistical homogeneity of the configurations required the use of many spherical windows. Indeed, there is no reason why the spherical window should be centered at a specific point.

In the present case, however, the configuration is not statistically homogeneous, and the center of the packing is the obvious choice for the center of the spherical window $\mathcal{W}$ (whose radius R is chosen so that $\mathcal{W}$ coincides with the sphere enclosing the packing). Similarly to Eq. (19), the scattering amplitude is then computed as follows:

$$A(\boldsymbol{q}) = \sum_{\beta=1}^{N} \Delta\rho_\beta v_\beta F_\beta(\boldsymbol{q}) \exp(-i\boldsymbol{q}\cdot\boldsymbol{x}_\beta) - \Delta\overline{\rho}|\mathcal{W}| \exp(-i\boldsymbol{q}\cdot\boldsymbol{x}) F_{\mathrm{w}}(\boldsymbol{q}),$$

where it should be noted that since all particles are completely included in $\mathcal{W}$, Eq. (19) is greatly simplified. The scattering intensity is then retrieved from $I(\boldsymbol{q}) = |\mathcal{W}|^{-1}|A(\boldsymbol{q})|^2$. Finally, sampling the directions of $\boldsymbol{q}$ allows the estimation of the isotropic average $I(q)$.

[1] A. Hasmy, E. Anglaret, M. Foret, J. Pelous, and R. Jullien, Phys. Rev. B **50**, 6006 (1994).
[2] L. D. Gelb and K. E. Gubbins, Langmuir **14**, 2097 (1998).
[3] L. D. Gelb and K. E. Gubbins, Langmuir **15**, 305 (1999).
[4] M. D. Rintoul and S. Torquato, J. Colloid Interface Sci. **186**, 467 (1997).
[5] C. L. Y. Yeong and S. Torquato, Phys. Rev. E **57**, 495 (1998).
[6] C. L. Y. Yeong and S. Torquato, Phys. Rev. E **58**, 224 (1998).
[7] S. Sankaran and N. Zabaras, Acta Mater. **54**, 2265 (2006).
[8] E. Patelli and S. Gerhart, Comput. Mater. Sci. **45**, 536 (2009).
[9] J. Pikunic, C. Clinard, N. Cohaut, K. E. Gubbins, J.-M. Guet, R. J.-M. Pellenq, I. Rannou, and J.-N. Rouzaud, Langmuir **19**, 8565 (2003).
[10] S. K. Jain, R. J.-M. Pellenq, J. P. Pikunic, and K. E. Gubbins, Langmuir **22**, 9942 (2006).
[11] R. Salazar and L. D. Gelb, Langmuir **23**, 530 (2007).
[12] J. J. Salacuse, A. R. Denton, and P. A. Egelstaff, Phys. Rev. E **53**, 2382 (1996).
[13] A. J. Allen, C. G. Windsor, V. Rainey, D. Pearson, D. D. Double, and N. M. Alford, J. Phys. D **15**, 1817 (1982).
[14] A. J. Allen, R. C. Oberthur, D. Pearson, P. Schofield, and C. R. Wilding, Philos. Mag. B **56**, 263 (1987).
[15] H. M. Jennings, Cem. Concr. Res. **30**, 101 (2000).
[16] H. M. Jennings, Mater. Struct. (Dordrecht, Neth.) **37**, 59 (2004).
[17] H. M. Jennings, Cem. Concr. Res. **38**, 275 (2008).
[18] H. M. Jennings, J. J. Thomas, J. S. Gevrenov, G. Constantinides, and F.-J. Ulm, Cem. Concr. Res. **37**, 329 (2007).
[19] M. Vandamme and F.-J. Ulm, Proc. Natl. Acad. Sci. USA **106**, 10552 (2009).
[20] M. Vandamme, F.-J. Ulm, and P. Fonollosa, Cem. Concr. Res. **40**, 14 (2010).
[21] R. J. M. Pellenq, A. Kushima, R. Shahsavari, K. J. Van Vliet, M. J. Buehler, S. Yip, and F.-J. Ulm, Proc. Natl. Acad. Sci. USA **106**, 16102 (2009).
[22] A. Guinier and G. Fournet, *Small-Angle Scattering of X-rays* (Wiley, 1955).
[23] G. Porod, in *Small Angle X-ray Scattering*, edited by O. Glatter and O. Kratky (Academic Press, London, 1982), Chap. 2, pp. 17–51.
[24] P. Debye, H. R. Anderson, Jr., and H. Brumberger, J. Appl. Phys. **28**, 679 (1957).
[25] L. C. Roess and C. G. Shull, J. Appl. Phys. **18**, 308 (1947).
[26] A. Denton and P. Egelstaff, Z. Phys. B: Condens. Matter **103**, 343 (1997).
[27] F. L. Román, J. A. White, and S. Velasco, J. Chem. Phys. **107**, 4635 (1997).
[28] M. Tomšič, A. Jamnik, G. Fritz-Popovski, O. Glatter, and L. Vlček, J. Phys. Chem. B **111**, 1738 (2007).
[29] A. Lajovic, M. Tomšič, and A. Jamnik, J. Chem. Phys. **133**, 174123 (2010).
[30] S. F. Parker and P. B. Tooke, Spectrochim. Acta, Part A **53**, 2245 (1997).
[31] D. Frenkel, R. J. Vos, C. G. de Kruif, and A. Vrij, J. Chem. Phys. **84**, 4625 (1986).
[32] J. J. Salacuse, A. R. Denton, P. A. Egelstaff, M. Tau, and L. Reatto, Phys. Rev. E **53**, 2390 (1996).
[33] N. E. Moe and M. D. Ediger, Phys. Rev. E **59**, 623 (1999).
[34] A. Donev, F. H. Stillinger, and S. Torquato, Phys. Rev. Lett. **95**, 090604 (2005).
[35] P. Welch, IEEE Trans. Audio Electroacoust. **15**, 70 (1967).
[36] P. C. Hansen, Numerical Algorithms **29**, 323 (2002).
[37] C. R. Vogel, *Computational Methods for Inverse Problems*, Frontiers in Applied Mathematics (SIAM, Philadelphia, 2002).
[38] P. C. Hansen, SIAM Rev. **34**, 561 (1992).
[39] P. C. Hansen and D. P. O'Leary, SIAM J. Sci. Comput. **14**, 1487 (1993).
[40] G. H. Golub, M. T. Heath, and G. Wahba, Technometrics **21**, 215 (1979).
[41] V. A. Morozov, *Methods for Solving Incorrectly Posed Problems* (Springer-Verlag, New York, 1984).
[42] M. P. Allen and D. J. Tildesley, *Computer Simulation of Liquids* (Oxford Science Publications, Oxford, 1987).
[43] B. J. Alder and T. E. Wainwright, J. Chem. Phys. **33**, 1439 (1960).
[44] L. V. Woodcock, J. Chem. Soc., Faraday Trans. 2 **72**, 1667 (1976).
[45] P. Levitz, J. Phys. Chem. **97**, 3813 (1993).
[46] B. D. Lubachevsky and F. H. Stillinger, J. Stat. Phys. **60**, 561 (1990).
[47] A. R. Kansal, S. Torquato, and F. H. Stillinger, J. Chem. Phys. **117**, 8212 (2002).
[48] A. Donev, S. Torquato, and F. H. Stillinger, J. Comput. Phys. **202**, 737 (2005).
[49] A. Donev, S. Torquato, and F. H. Stillinger, J. Comput. Phys. **202**, 765 (2005).
[50] N. Metropolis, A. W. Rosenbluth, M. N. Rosenbluth, A. H. Teller, and E. Teller, J. Chem. Phys. **21**, 1087 (1953).
[51] S. Kirkpatrick, C. D. Gelatt, and M. P. Vecchi, Science **220**, 671 (1983).

[52] J. W. Perram and M. S. Wertheim, J. Comput. Phys. **58**, 409 (1985).
[53] D. N. Winslow, Cem. Concr. Res. **15**, 817 (1985).
[54] D. Pearson and A. J. Allen, J. Mater. Sci. **20**, 303 (1985).
[55] A. J. Allen, J. Appl. Crystallogr. **24**, 624 (1991).
[56] D. N. Winslow, J. M. Bukowski, and J. F. Young, Cem. Concr. Res. **24**, 1025 (1994).
[57] R. Maggion, S. Bonnamy, P. Levitz, and H. Vandamme, in *The Modeling of Microstructure and its Potential for Studying Transport Properties and Durability*, edited by H. M. Jennings, J. Kropp, and K. Scrivener (Springer, 1995), pp. 137–155.
[58] D. Winslow, J. M. Bukowski, and J. F. Young, Cem. Concr. Res. **25**, 147 (1995).
[59] A. J. Allen and R. A. Livingston, Adv. Cem. Based Mater. **8**, 118 (1998).
[60] J. J. Thomas, H. M. Jennings, and A. J. Allen, Cem. Concr. Res. **28**, 897 (1998).
[61] J. J. Thomas, H. M. Jennings, and A. J. Allen, Adv. Cem. Based Mater. **7**, 119 (1998).
[62] J. J. Thomas, J. J. Chen, A. J. Allen, and H. M. Jennings, Cem. Concr. Res. **34**, 2297 (2004).
[63] A. J. Allen and J. J. Thomas, Cem. Concr. Res. **37**, 319 (2007).
[64] J. J. Thomas, A. J. Allen, and H. M. Jennings, J. Am. Ceram. Soc. **91**, 3362 (2008).
[65] J. J. Thomas, A. J. Allen, and H. M. Jennings, J. Phys. Chem. C **113**, 19836 (2009).
[66] French Institute of Science and Technology for Transport, Development, and Networks.
[67] R. E. Beddoe and K. Lang, Cem. Concr. Res. **24**, 605 (1994).
[68] A. Heinemann, H. Hermann, and F. Häussler, Physica B (Amsterdam, Neth.) **276–278**, 892 (2000).
[69] P. Meakin, Phys. Rev. A **38**, 4799 (1988).
[70] S. Tang, J. M. Preece, C. M. McFarlane, and Z. Zhang, J. Colloid Interface Sci. **221**, 114 (2000).
[71] P. S. Dodds and J. S. Weitz, Phys. Rev. E **65**, 056108 (2002).
[72] M. Borkovec, W. De Paris, and R. Peikert, Fractals **2**, 521 (1994).
[73] P. Levitz and D. Tchoubar, J. Phys. I **2**, 771 (1992).
[74] J. K. Kjems, T. Freltoft, D. Richter, and S. K. Sinha, Physica B + C (Amsterdam) **136**, 285 (1986).
[75] J. E. Martin and A. J. Hurd, J. Appl. Crystallogr. **20**, 61 (1987).
[76] P. W. Schmidt, in *The Fractal Approach to Heterogeneous Chemistry*, edited by D. Avnir (John Wiley and Sons Ltd., Chichester, 1989), pp. 67–79.
[77] S. Torquato, *Random Heterogeneous Materials: Microstructure and Macroscopic Properties* (Springer-Verlag, New York, 2002).
[78] *Handbook of Mathematical Functions*, edited by M. Abramowitz and I. A. Stegun (Dover, New York, 1965).
[79] I. S. Gradshteyn and I. M. Ryzhik, *Table of Integrals, Series, and Products*, 7th ed. (Academic Press, 2007).